The intrinsic nature of antigorite breakdown at 3 GPa: Experimental constraints on redox conditions of serpentinite dehydration in subduction zones

Juliette Maurice, Nathalie Bolfan-Casanova, Sylvie Demouchy, Paul Chauvigne, Federica Schiavi, Baptiste Debret

The intrinsic nature of antigorite breakdown at 3 GPa: Experimental constraints on redox conditions of serpentinite dehydration in subduction zones

Juliette MAURICE[1], Nathalie BOLFAN-CASANOVA[1]*, , Sylvie DEMOUCHY[2], Paul CHAUVIGNE[1], Federica SCHIAVI[1], Baptiste DEBRET[3],

[1] Laboratoire Magmas et Volcans, Campus des Cézeaux, 6 Avenue Blaise Pascal, 63178 Aubière, France.

[2] Géosciences Montpellier, CNRS & Université Montpellier, Place E. Bataillon, 34095, Montpellier, France.

[3] Laboratoire G-Time, DGES, Université Libre de Bruxelles, ULB, CP 160/02, 1050, Brussels, Belgium.

*corresponding author: nathalie.bolfan@uca.fr

Accepted to Contrib. Min. Petrol.

12 August 2020

Abstract

Antigorite is considered as the most important source of water in subduction zones, playing a key role during arc magma genesis. Although, these magmas seem more oxidized than mid-oceanic ridge basalts (MORB), the possible inherent link between the oxidation state of arc magmas and serpentinite-derived hydrous fluids is still not well established. Here, we have performed dehydration experiments of natural antigorite serpentinite containing 5 weight percent (wt%) magnetite at 3 GPa and in a temperature range from 600 to 900 °C using a multi-anvil apparatus. These experiments aim to reproduce the different stages of H_2O release, forming chlorite, olivine and orthopyroxene and water. Our experimental set up permits to preserve the intrinsic oxygen fugacity (fO_2) of serpentinites during their dehydration. The new olivine and orthopyroxene which formed in equilibrium with antigorite, chlorite and magnetite have high X_{Mg} numbers setting up the oxygen fugacity to high values, between 3.0 and 4.1 log units above QFM (Quartz-Fayalite-Magnetite buffer). Hematite is observed concomitantly with high X_{Mg} in olivine, of 0.94-0.97, generally at low temperatures, below 800 °C, in coexistence with chlorite. Once the magnetite is destabilized, upon chlorite breakdown, above 800°C, the oxygen fugacity decreases to 3.7 due to the decrease of the X_{Mg} of silicates. This study demonstrates the highly oxidizing nature of the fluids released from antigorite dehydration. Thus, at high pressure and high temperature conditions, fO_2-sensitive elements such as carbon and sulfur are expected to be mobilized under their oxidized form, providing an oxidizing context for arc magmas genesis and assuming that they are not completely reduced by their percolation through meta-gabbro, meta-basalts and meta-sediments.

Key words: antigorite, serpentinites, peridotite, subduction, high-pressure research, oxygen fugacity

INTRODUCTION

Subduction of oceanic lithosphere is associated with material recycling in the mantle. In particular, the release of volatiles, such as H_2O, induces partial melting of the mantle wedge and is at the origin of arc magmatism (e.g. Ulmer and Trommsdorff, 1995; Schmidt and Poli, 1998; Gaetani and Grove, 1998; Grove et al., 2006; Plank and Langmuir, 1998). While hydrous lithologies among pelagic sediments and meta-basalts mostly dehydrate at relatively shallow depth in the fore-arc region (approximately 100 km of depth, e.g., Tatsumi, 1986), ultramafic hydrated lithologies, such as serpentinites, can release large amounts of water at greater depths (150-200 km, Ulmer and Trommsdorff, 1995). Serpentinites are rocks formed by the hydrothermal alteration and oxidation of Mg-rich silicates composing peridotites; they are mostly composed of serpentine, which is a layered and hydrous phyllosilicate, plus a few percent of magnetite. Serpentinization of ultramafic rocks occurs in different geological settings: for example: on the oceanic seafloor of slow and ultra-slow spreading ridges (e.g., Cannat et al., 1990; Mevel, 2003), at slab bending related faults (Ranero et al., 2003) and at the mantle wedge – slab interface when slab-related fluids are released (Deschamps et al., 2010; Guillot et al., 2000), rendering serpentinites ubiquitous in subduction zones (see Reynard et al., 2013; Guillot et al., 2015). Antigorite, the high temperature and high pressure serpentine variety (Evans et al., 1976; Mellini et al., 1987; Schwartz et al., 2013), is considered as the most important water carrier within the down-going lithospheric plate, as it is the most abundant hydrous silicate in ultramafic lithologies and the most hydrous with up to 12 wt.% H_2O. Therefore, antigorite breakdown which occurs upon slab subduction and thermal relaxation is the primary source of subduction-related aqueous fluids (Ulmer and Trommsdorff, 1995; Schmidt and Poli, 1998, 2014).

In addition to water release from the slab and its transfer to the mantle wedge, the speciation of the primary fluids will be controlled by the redox state of the rock from which they originate. The redox budget of serpentinite in subduction zones can be estimated using the $Fe^{3+}/\Sigma Fe$ ratio of the bulk rock (e.g., Evans, 2006, 2012; Evans and Tomkins, 2011; Evans and Powell 2015; Tumiati et al., 2015), as well as the content and speciation of C and S. What are the consequences of subducting a relatively oxidized serpentinized peridotite on the oxidation state of the fluids produced and the implications for the sub-arc mantle?

Samples of exhumed high-pressure serpentinites from ophiolites have allowed petrological characterization of antigorite dehydration reaction in natural settings**.** For instance, natural serpentinites from Cerro del Almirez (Debret et al., 2015; Garrido et al., 2005; López Sánchez-Vizcaíno et al., 2005; Padrón-Navarta et al., 2010a, 2010b, 2011; Trommsdorff et al., 1998, Brestcher et al. 2018, Piccoli et al. 2019) and Cima di Gagnone (e.g., Evans and Trommsdorff, 1978; Scambelluri et al., 2014, Piccoli et al. 2019) have helped constraining the reaction of antigorite destabilization into chlorite then olivine + enstatite nominally anhydrous assemblage. However, as discussed in the petrological models of Evans and Powell (2015) magnetite is the phase controlling the redox budget of serpentinite.

In addition to magnetite, occurrence of hematite in mafic and ultramafic lithologies from the Western Alps (e.g., Philippot and Selverstone, 1991; Debret et al., 2016) suggests that high fO_2, with values between QFM (Quartz-Fayalite-Magnetite buffer assemblage) +2 and more than +5, can be reached during antigorite breakdown (Debret and Sverjensky, 2017), thus even above the hematite-magnetite buffer. Still, hematite had never been observed in experimental assemblages. This study aims to investigate the conditions of formation of hematite during antigorite dehydration.

Until recently, no experimental study was considering the fate of the iron oxide, namely magnetite, which accounts for ~ 5 wt.% of the bulk rock in most of serpentinites, at least in

mid-ocean ridge settings (Andreani et al., 2013; Klein, 2014). Merkulova et al. (2016, 2017) are the first to perform serpentine dehydration experiments focusing on the evolution of magnetite. Mixes of powdered natural antigorite and commercial magnetite were equilibrated at 1.5 to 2 GPa and different temperatures from 450 to 900 °C in graphite furnaces using the piston cylinder device. Their results point out to fluids being released at an oxygen fugacity of QFM-2, buffered by the graphite furnace. While Iacovino et al. (2020) monitored the oxygen fugacity during the dehydration of a natural serpentinite in the piston cylinder at 1 GPa and 800 °C using an f_{O2} sliding sensor Ni_xPd_{1-x}. They measured a significantly higher oxygen fugacity of QFM+2.

Thus, here, we examine the intrinsic oxygen fugacity of natural serpentinite after antigorite breakdown by performing high-pressure experiments in a multi-anvil press at 3 GPa and 600 to 900 °C. In a first series of experiments, we dehydrated a cylinder sample of natural serpentinite containing 5 wt.% magnetite in contact with a layer of sintered San Carlos olivine, which acts as a fluid trap. In these experiments, hematite was produced. In following experiments, powdered samples were used, with or without olivine trap. The conditions imposed to the sample were also varied such as temperature, heating duration, capsule material or even furnace material. Initially, such experiments intended to let the sample evolve in a closed system as much as possible, by using a passive environment with respect to the redox state of the starting material. The aim was to understand the key parameter controlling the formation of hematite during serpentinite dehydration experiments.

MATERIAL & METHODS

Natural antigorite sample

Experiments were conducted using a natural serpentinite from the Iron Mountain, North Cascades, Washington, USA. The serpentinite is composed of a matrix of pure antigorite and oxides from the spinel group (Figure 1). No olivine, calcium-rich phases (diopside or tremolite) nor nickel-alloys have been observed in the investigated starting sample. To avoid H_2O and CO_2 absorption expected to occur when grinded material is used, our starting sample was first prepared by drilling a cylinder from the rock specimen. Subsequently, to test whether equilibrium was attained in the experiments using cylinders, we also used powdered serpentinite. A sample from the same locality was investigated by Evans (2012, sample #IM3) using Mössbauer spectroscopy, yielding a $Fe^{3+}/\sum Fe$ ratio of 0.23 for the antigorite. The same value is assumed in this study. The composition of antigorite $Mg_{2.62}Fe^{2+}_{0.08}Fe^{3+}_{0.02}Al_{0.09}Cr_{0.01}Si_{1.97}O_{6.82}(OH)_{3.65}$ was obtained by means of an electron probe micro-analyzer and a $Fe^{3+}/\sum Fe$ ratio of 0.23. The calculated water content (12.05 wt.% H_2O) by stoichiometry) was obtained for an anticipated polysome (m = 17, Capitani and Mellini, 2004) in agreement with the totals of electron probe analysis ranging around 86.5 +/- 0.5 %, see (Table 1, see also Maurice et al., 2018). Bulk analyses were performed using inductively coupled plasma atomic emission spectroscopy (ICP-AES) on 5 distinct batches of about 100 mg of serpentinite powder, separately grinded, in order to test the homogeneous distribution of magnetite grains within the bulk rock. The average of measurements of the bulk rock composition (BR_1) is reported in Table 1, as well as the standard deviation calculated from the 5 analyses. The only marginally higher amount of chromium in BR_1 (0.27 wt% Cr_2O_3) compared to antigorite (0.22 wt% Cr_2O_3), indicates a very minor proportion of chromite and associated spinel (<<1%). Therefore, here, the redox budget of the bulk rock is determined by the modal amount of magnetite (Figure 1a). Mass balance calculation based on the total iron content in the bulk rock (7.79 +/-0.48 wt.% FeO_{total}), in magnetite (91.32 wt.% FeO_{total}) and in antigorite (2.6 wt.% FeO_{total} with a $Fe^{3+}/\sum Fe$ ratio = 0.23) indicates that the sample contains up

to 5.5 % magnetite in average, in agreement with analyses of backscattered images (as shown in Figure 1a). It follows a calculated bulk rock composition, BR_2, made of 5.5 wt.% magnetite and 94.5 wt.% antigorite yielding a ratio of $Fe^{3+}/\sum Fe = 0.52$ (Table 1). The water content of the bulk rock was estimated by loss on ignition and equals to 11.40 wt.% H_2O, which agrees with an antigorite content in the bulk rock of 94.5 %. The sulfur content has been measured using the Flash 2000 CHNS-O elemental analyzer from Thermo Fisher Scientific equipped with a 'MAS 200R' autosampler and reaches 150 ppm wt of S. The composition of the serpentinite used here is similar to the one from Cerro del Almirez (Padrón-Navarta et al., 2010, 2011) or from the Voltri Massif in the Alps (Iacovino et al., 2020), both are reported in Table 1 for comparison. The composition is also similar to the average of serpentinites reported worldwide (see Iacovino et al., 2020, their Fig. 2).

The matrix of antigorite is dense, with rare porosity displayed in Figure 1, due to thin section preparation. Two different occurrences of spinel group minerals have been observed: small grains of pure magnetite (100 μm in length) and oxide overgrowths displaying Cr-spinel-rich cores surrounded by chromite-rich and mantled by magnetite (Fig. 1b). These oxides occur as large aggregates, up to 900 μm in length. This type of oxides clusters is typical of serpentinites (e.g., Gervilla et al., 2012; Debret et al., 2014, their Fig. 3). Magnetite displays a composition close to the end-member. Despite intensive search, no pre-existing hematite was observed in the starting antigorite.

As already mentioned above, three types of starting material were used in this study (see Table 2). In the first experiments, an intact serpentinite cylinder was used together with a sintered polycrystalline olivine, acting as a fluid trap. The initial objective of the trap was to look at the interaction of a serpentinite and released fluid with an overlying wedge mantle, modeled here as dunite. However, this objective is beyond the scope of this paper and we focus here on the characterization of the oxygen fugacity experienced by the serpentinite during

dehydration. In the second series of experiments we used powder of serpentinite together with a powder olivine trap. In the third series of experiments, we used only serpentinite powder without olivine trap. In this last series, we also varied the capsule material (AuPd or Au) and tested the presence/absence of magnetite in the starting material (the initial rock was grinded and magnetite was separated with a magnet). In addition, to evaluate the effect of volatile species on the redox potential of the fluids expelled from antigorite dehydration, we also performed two additional experiments where we added Cl (in the form of NaCl, 1 wt%) and S (in the form of FeS, 1 wt.%), mixed with the serpentinite powder.

High-pressure experiments

Breakdown of antigorite was performed using a multi-anvil press at 3 GPa and 600 to 900 °C with varying run durations. The multi-anvil apparatus was preferred over piston-cylinder because of furnace versatility. Experimental conditions are reported in Table 2. Experiments were conducted with 25 and 18 mm edge length octahedra made of MgO + 5% Cr_2O_3 and WC cubes of 32 mm edge with 17 and 11 mm truncation, respectively. The pressure in the 25 mm assembly was calibrated using three systems: (i) Bi I-II phase transition occurring at 2.5 GPa and room temperature (Bean et al., 1986), (ii) the coesite/stishovite phase transition of SiO_2 at 8.01 GPa at 800 °C (Zhang et al., 1996) and (iii) the garnet to perovskite phase transition of $CaGeO_3$ at 6.2 GPa and 1000 °C (Susaki et al., 1985). For experiments using the 18/11 assemblies see (Maurice et al., 2018). All the ceramic parts (except graphite) of the high-pressure cell were fired at 1000 °C for 30 minutes prior to loading the capsule and cementing.

The samples were placed in noble metal capsules, $Au_{80}Pd_{20}$ or Au (length: 4.3 mm, diameter: 3 mm, in the 25M assembly; length: 2.7 mm, diameter: 2 mm for the 18M assembly; wall thickness: 0,35 mm), which is then arc-welded at the top and bottom. The capsule was

insulated from the furnace by an MgO sleeve. We also used the Ni_xPd_{1-x} oxygen fugacity sensor following Matjuschkin et al. (2015). We mixed a 1:1 molar NiO and Pd powder with 3 µl of water which was inserted in an alumina tube tapped with alumina powder in order to be insulated from the Pt capsule (instead of AuPd or Au capsule in order to avoid contamination of the sensor by Au). This experiment was held at 800 °C and 3 GPa for 5 hours (#M865). The equilibration of Ni_xPd_{1-x} sensor at 800 °C and 3 GPa for 5 hours, yields X_{Ni} alloy of 0.25 in mole fraction, equivalent to a log(f_{O2}) of -11.3 bars.

The furnace was in most experiments made of $LaCrO_3$ and two experiments used C (graphite) to test whether the furnace alters the oxygen fugacity within the sample during the time of the experiment. The furnace shape was stepped to reduce thermal gradients along the capsule. Temperature was measured using a Pt/Rh thermocouple in contact with the capsule. The thermal gradient was simulated using the finite element method by Hernlund et al. (2006) and yields a thermal gradient less than 30 °C/mm when using $LaCrO_3$ furnace and less than 11 °C/mm when using graphite furnace. The final pressure was obtained following a steady increase ramp within 2 hours to reach 3 GPa and pressure was maintained constant for 3 to 24 hours (Table 2). Turning off the power quenched the experiments and the pressure was automatically decreased over 8-9 hours (i.e., slow decompression) to minimize cracks formation.

Characterization of run products

After the experiments, the capsules were embedded in a dental resin and gently hand-polished with 1200 µm grid silicon carbide paper, then polished using 6, 3 and ¼ µm diamond paste and subsequently carbon coated prior to chemical analyses. First, chemical characterization was performed using a scanning electron microscopy (SEM) and Energy-dispersive X-ray

spectroscopy (EDS) mapping. Then, electron probe microanalyses (EPMA) were performed to obtain the chemical composition of the products of antigorite dehydration. The beam current and intensity was set to 15 keV and 15 nA, respectively, for olivine and enstatite and the intensity was lowered to 8 nA for antigorite and other hydrous minerals. A point beam set up (1 μm in diameter) was used.

Regular settings of the EPMA analyses were modified for the iron oxides to allow quantification of oxygen using hematite or magnetite as standards. Detection of Ti and Cr was performed with pentaerythritol (PET) diffraction crystal, oxygen with the pseudo-crystal 1 (PC1), Fe and Mn with the lithium fluoride (LIF) crystal, and Al and Mg with the thallium acid phthalate (TAP) crystal. For regular silicates analyses, oxygen is only calculated from stoichiometry, the rest of the elements are detected on the same diffraction crystals with addition of Ca, Ni (LiF), Si. Magnetite end member displays an oxygen/Σcations ratio of 1.33, while the ratio for hematite is equal to 1.50, as confirmed by analyzing the standards of magnetite and hematite used for EPMA calibration. It allowed the identification of these two phases in the experimental samples. Data were normalized to 4 oxygens for spinel group minerals, and to 3 oxygens for hematite (see Table 4).

To confirm independently the identification of hematite and magnetite, Raman spectroscopy was performed on the oxides. Raman spectra were collected at Laboratoire Magmas et Volcans (Clermont–Auvergne-Université) using an InVia confocal Raman micro-spectrometer manufactured by Renishaw and equipped with a 532 nm diode laser (200 mW output power), a Peltier-cooled charge-coupled device (CCD) detector, a motorized XY stage and a Leica DM 2500M optical microscope. Scattered light was collected by a backscattered geometry. Laser power on the experimental samples was reduced by filters in order to operate ≤ 0.7 mW to avoid thermal oxidation of magnetite into hematite (de Faria et al., 1997). A 100× microscope objective and 20 μm slit aperture were used along with a 2400 grooves/mm grating,

which resulted in a spectral resolution better than 1 cm^{-1}. Daily calibration of the spectrometer was performed based on the most intense peak of Si located at 520.5 cm^{-1}. The spectra were recorded from 100 to 1800 cm^{-1} in extended mode using the Wire 4.2 software. Acquisition time was set to 120 s. After each analysis, the surface of the experiment has been checked using an optical microscope in reflective light to ensure that the minerals have not been damaged nor oxidized by the laser during the analyses.

RESULTS

Textural and chemical evolution of the dehydration products

Different silicates and oxides assemblages (all H_2O saturated) were found as a result of increasing temperature. Run conditions and product phases are reported in Table 2 and in a pressure-temperature diagram in Figure 2. The compositions in major elements in all co-existing silicate phases are reported in Table 3. Oxides major elements compositions are reported in Table 4. At 3 GPa, antigorite is stable at a temperature up to 690 °C, in agreement with the stability field of antigorite presented in previous studies (e.g., Bose and Navrotsky, 1998; Bromiley and Pawley, 2003; Padrón-Navarta et al., 2010a; Ulmer and Trommsdorff, 1995; Wunder and Schreyer, 1997). Each reaction stage is detailed below, first for the silicate components followed by the co-existing oxides.

Silicates

After partial dehydration at 680 and 690 °C, antigorite coexists with chlorite, olivine, enstatite and water. The texture displays high porosity (10 %) with tabular Atg (10 to 80 µm long) and xenomorphic chlorite + olivine + enstatite (10 µm size maximum, see Figure 3a). Enstatite is

characterized by needle-like crystals, either well defined or inter-grown with olivine (see Figure 3a and 3c). Pyroxene crystals are often very small and thin, thus quite difficult to analyze. Chlorite is easily identified in EDS maps due to its high alumina content as illustrated in Figure 3b, it crystallizes as interstitial small grains (5-10 μm width) coexisting with olivine and orthopyroxene.

At temperatures above or equal to 700 °C, antigorite is completely transformed into chlorite + olivine + enstatite + H_2O. The product assemblage consists in a aggregate of small rounded crystals of olivine (5-10 μm) inter-grown with acicular to needle-like enstatite prisms (up to 30 μm in length). The composition of chlorite is close to clinochlore $(Mg,Fe)_5Al(Si_3Al)O_{10}(OH)_8$. When chlorite coexists with antigorite, chlorite contains 12.4-12.9 wt. % Al_2O_3. Once antigorite breaks down, chlorite becomes enriched in aluminum with concentration up to 13-15.5 wt. % Al_2O_3 (see Figure 4).

At temperatures at or above 800 °C, the hydrous phases have completely disappeared and only the nominally anhydrous olivine and enstatite remain +/- the oxides (see Figures 3c,d). No garnet is observed in the mineral assemblage and this absence is probably due to the refractory character of the protolith which has relatively a low alumina content (1.6 wt.% Al_2O_3) as well as the fact that most of the Al can be accommodated in the enstatite (with contents that vary from 1.7 +/- 0.2 at 680 °C to 5.0 +/- 0.8 wt% Al_2O_3 at 900 °C). The incorporation of Al in the pyroxene seems to follow a Tschermak's substitution ($Mg^{2+}+Si^{4+} = 2Al^{3+}$) as shown in Figure 5).

The X_{Mg} of olivine is on average 0.96 +/- 0.01 at temperatures ≤ 850 °C (see Figure 6), close to the X_{Mg} of the starting antigorite (0.96, see Table 1) and of chlorite (X_{Mg} ~0.95). In the two samples where magnetite was removed from the starting serpentinite powder (#830 and #897A), olivine displays high X_{Mg} ranging from 0.93 to 0.96. With increasing temperature (i.e. above 800 °C) magnetite breaks down and olivine incorporates more iron and consequently its

X_{Mg} decreases down to 0.88-0.89 (#827, #832, #897B). In one sample which was heated at a higher temperature of 850 °C for 12 hours, (#737), no magnetite is observed anymore and olivine composition is homogeneous with X_{Mg} = 0.89, close to that of mantle olivine i.e. similar to the potential protolith before serpentinization. Coexisting orthopyroxene usually have X_{Mg} values ranging from 0.94 +/- 0.2. In any case, the partitioning of iron between olivine and orthopyroxene follows the same trend, although with some scatter, maybe owing to the aluminum incorporation in orthopyroxene as observed by von Seckendorf and O'Neill (1987) at higher temperatures, (see discussion and supplementary Figure 1a).

Oxides

The different oxides (chromite spinel, magnetite, hematite) are easily distinguished by their different optical properties in reflected light (see Supplementary Figure 2). Their structure was confirmed by Raman spectroscopy (Figure 7) and their chemical composition by electron microprobe (Table 4, and Figure 8). Optically zoned chromite grains display the common Fe-rich rim with higher reflectance, i.e. the grains consist of a dark core surrounded by a rim that changes gradually in composition (enriched in Fe and depleted in Mg, Al and Cr) towards magnetite at the border. The cores are relatively homogeneous in composition and are inherited from the protolith (see Figure 1 and 8; Bliss and MacLean, 1975, Gervilla et al., 2012). The average compositions representing these three poles are $(Mg_{0.55}Fe_{0.5})(Al_{1.14}Cr_{0.8})O_4$ for the core, $(Mg_{0.08}Fe_{0.92})(Fe_{1.05}Al_{0.06}Cr_{0.8})O_4$ for the intermediate ferri-chromite to $(Mg_{0.1}Fe_{0.9})(Fe_2Al_{0.001}Cr_{0.04})O_4$ in the magnetite rim. This magnetite rim has been recognized to form during serpentinization or prograde metamorphism (Bliss and MacLean, 1975; Burkhard, 1993, Gervilla et al., 2012). The composition of magnetite varies from $(Fe_{0.72}Mg_{0.28})(Fe_{1.96}Cr_{0.03})O_4$ to $Fe_{2.94}Cr_{0.04}O_4$ (see Table 4).

Presence /absence of hematite

In several experiments hematite is observed as lamellae crossing pre-existing magnetite grains as shown in Figure 7 or supplementary Figure 2. The composition of hematite varies from $Fe_{1.92}O_3$ to $Fe_{1.97}O_3$. Hematite is observed concomitantly with high X_{Mg} in olivine, of 0.94-0.97 (see Figure 6). These features usually occur at temperatures below 800-850 °C, often in coexistence with antigorite and/or chlorite. Hematite is not observed in experiments using graphite furnace at 700 and 900 °C. It is mostly observed in AuPd-capsules but also in one Au-capsule experiments (#900B, see Table 2). It is observed in presence or in absence of olivine trap.

Oxygen fugacity prevailing during the experiments

The oxygen fugacity can be constrained using the silicate phase assemblage when either hematite or magnetite are stable. In experiments where hematite was observed, the oxygen fugacity, f_{O2}, can be calculated using the equilibrium between quartz, fayalite and hematite (QFH):

$$2\ Fe_2SiO_4 + O_2 = 2\ SiO_2 + 2\ Fe_2O_3 \quad (1)$$

It follows

$$\log f_{O2} = 2 \log a_{SiO2} + 2 \log a^{hematite}_{Fe2O3} - 2 \log a^{olivine}_{Fe2SiO4} + \Delta G_1/(\ln(10).RT) \quad (2)$$

where R is the real gas constant and T is temperature in Kelvins. The activity of silica was calculated using the equilibrium between the magnesian endmembers of olivine and pyroxene, following Stagno and Frost (2010):

$$Mg_2SiO_4 + SiO_2 = Mg_2Si_2O_6 \quad (3)$$

i.e.

$$\log a_{SiO2} = \log a^{orthopyroxene}_{Mg2Si2O6} - \log a^{olivine}_{Mg2SiO4} + \Delta G_3/(\ln(10).RT) \quad (4)$$

The Gibbs energies were calculated using the thermodynamic parameters of the end-members of the solid solutions (see Table 5) and using the activities, a_i, of the end-members in the phases a_{SiO2}, $a^{orthopyroxene}_{Mg2Si2O6}$, $a^{olivine}_{Mg2SiO4}$, $a^{olivine}_{Fe2SiO4}$, which were calculated from Table 3 using the expressions of the activity coefficients given in Table 5. The samples are compared throughout all this study to the QFM buffer that was also calculated at 3 GPa and 660 to 900 °C using the thermodynamic database in Table 5, to obtain internally consistent oxygen fugacity values. Our calculation of QFM agrees within 0.4 log units of the formulation of QFM provided by Ballhaus et al. (1991) and O'Neill et al. (1987) from 600 to 1000 °C.

The oxygen fugacities of the samples calculated using the above QFH equilibrium, range between 3.1 and 4.1 log units above QFM (see Table 2 and Figure 9). The oxygen fugacity increases slightly with increasing temperature in the chlorite stability field and then decreases with decreasing X_{Mg} of olivine. Once chlorite disappears between 800 and 850 °C, the oxygen fugacity continues to decreases from 4.1 to 3.7 log units above QFM.

Attainment of equilibrium

We are able to confirm the attainment of local equilibrium in most experiments, as evidenced by the change in mineral compositions with experimental conditions, in particular the increase in Al content in orthopyroxene and chlorite with increasing temperature (see Figure 4). However, if we use the exchange of iron between olivine and orthopyroxene, as defined in reaction (5) below, we can identify samples that depart from the trend established

experimentally for mixes of olivine and enstatite at 900, 1000 and 1100 °C at 1.6 GPa (von Seckendorf and O'Neill, 1987, see Supplementary Figure1b):

$$Mg_2SiO_4 + Fe_2Si_2O_6 = Fe_2SiO_4 + Mg_2Si_2O_6 \quad (5)$$

The exchange partition coefficient of Fe between olivine and orthopyroxene can be defined:

$$Kd_{Fe\text{-}Mg}^{Ol/Opx} = (X_{Fe}^{Ol} .X_{Mg}^{Opx}.)/ (X_{Mg}^{Ol}. X_{Fe}^{Opx}) \quad (6)$$

Microprobe analysis of the run products indicate a $Kd_{Fe\text{-}Mg}^{Ol/Opx}$ varying between 0.5 to 1.9, while expected values should lie around 1. Note that for the samples where magnetite was removed from the starting material $Kd_{Fe\text{-}Mg}^{Ol/Opx}$ is of 1.1. Most samples of this study follow the partitioning of iron between olivine and orthopyroxene close to 1.0 +/- 0.2 as shown in Supplementary Figure 1b. However, there are some outliers that show very high values of 1.5 to 1.9 or very low values of 0.5 to 0.8. The high values of $Kd_{Fe\text{-}Mg}^{Ol/Opx}$ correspond to samples where destabilization of magnetite was readily observed, *i.e.* when magnetite was dissolving into silicates. While the low values of $Kd_{Fe\text{-}Mg}^{Ol/Opx}$ correspond to some samples that were coexisting with hematite (#900A, #900B, #869). Thus, for these three samples, the calculated oxygen fugacity is probably largely unconstrained, so they were removed from the discussion in Figure 9. Even if we discard the experiments with anomalous $Kd_{Fe\text{-}Mg}^{Ol/Opx}$, and only keep the experiments which display $Kd_{Fe\text{-}Mg}^{Ol/Opx}$ of 1.0+/- 0.2, we find that the products of dehydration of natural antigorite display log(f_{O2}) values between 3.1 and 4.1 relative to the QFM buffer.

DISCUSSION

Antigorite stability field

The present starting antigorite is Fe- and Al-poor compared to the natural specimens from Cerro del Almirez previously studied by Debret et al. (2015) and Padrón-Navarta et al. (2008, 2011) (see Table 1) and from others experimental compositions. Thus, as expected, we found small variations of the stability field of antigorite. For example, Ulmer and Trommsdorff (1995) investigated the antigorite breakdown of a material composed of a mixture of 85 volume percent (vol %) of natural antigorite (1.30 wt. % Al_2O_3, 2.94 wt% FeO) and 15 vol % brucite, to which was added 10 wt% of the dehydration products olivine + enstatite resulting from a preliminary experiment at high pressure and high temperature. Their work suggests a temperature of antigorite stability up to 690 °C at 3 GPa (see Figure 2a). Later on, Wunder and Schreyer (1997) first performed dehydration experiments on a synthetic antigorite gel in the MgO-SiO_2-H_2O system, then mixed the reaction products olivine + enstatite with natural antigorite powder in a 1:1 ratio and added ~ 20 wt.% H_2O. These experiments constrain the stability limit of antigorite (0.68 wt.% Al_2O_3, 1.66 wt.% FeO in the bulk) around 640 °C at 2.8 GPa and 650 °C at 3.5 GPa. Bromiley and Pawley (2003) bracketed the destabilization of antigorite at 3 GPa between 620 and 660 °C for experiments in the MgO-SiO_2-H_2O (MSH) system with 0.10 wt.% Al_2O_3 and 0.30 wt.% FeO (natural antigorite with synthetic olivine + synthetic enstatite + 20 wt.% water) and between 660 and 700 °C in the MgO-Al_2O_3-SiO_2-H_2O (MASH) system with 3.06 wt.% Al_2O_3 and 5.47 wt.% FeO (natural antigorite with synthetic olivine + enstatite + chlorite + 20 wt.% water). Similar experiments were conducted by Padrón-Navarta et al. (2010a) and show that complete dehydration of serpentine from Cerro del Almirez (3.10 wt.% Al_2O_3 and 6.56 wt% FeO) occurred between 665 and 680 °C and 2.5 - 1.9 GPa. These experimental studies have highlighted the thermal stabilizing effect of Al in Atg. On the other hand, it has been suggested that the incorporation of iron reduces the thermal stability field of antigorite. Indeed, Merkulova et al., (2016) have concluded that + 10 wt% FeO induced a decrease of about 25 °C for antigorite breakdown temperature, when compared to an iron-free system (i.e., 675 °C

instead of 700 °C, at 2 GPa). In our study, we found that the dehydration of natural Atg-rich serpentinite containing 2.62 wt% FeO and 1.66 wt% Al_2O_3 occurs between 660 and 680 °C at 3 GPa (Figure. 2a). Thus, in agreement with previous thermal stability limits proposed for various Al- and Fe-bearing compositions representative of serpentinized mantle materials mentioned above (e.g., Bromiley and Pawley, 2003; Merkulova et al., 2016; Padrón-Navarta et al., 2010a; Ulmer and Trommsdorff, 1995).

Open versus closed system

To perform hydrous experiments in a perfectly closed system is difficult. Actually, as long as H_2 is produced somewhere in the assembly, a gradient due to inhomogeneity in H_2 potential will force H_2 to diffuse in or out of the more or less permeable capsule. Therefore, a closed system can certainly not be maintained for a long time (see Truckenbrodt et al., 1997), and this is why we intended to keep the heating duration short (Table 2). Compared to the previous study of Merkulova et al. (2016), we do not observe disappearance of magnetite after antigorite starts dehydrating at low temperatures of 550 °C, but instead we observe the appearance of hematite. Magnetite in our experiments is stable up to ~800 °C. Given that our starting materials are similar (95% antigorite+5% magnetite), the reasons for the different observations must arise from different experimental strategies. We used mainly $LaCrO_3$ furnace, $Au_{80}Pd_{20}$ capsule and short duration experiments instead of graphite furnace, Au capsule and long duration experiments in their case. We examine below the effect of changing these three parameters on the parageneses obtained in our study.

i-Effect of the furnace material

We have monitored the oxygen fugacity imposed by the $LaCrO_3$ furnace in one experiment performed at 800 °C and 3 GPa. The value of oxygen fugacity is around QFM, showing that the f_{O2} imposed by the furnace is lower than that of the sample, around QFM+3 to +4. This means that the oxygen fugacities observed here are intrinsic of the serpentinite sample.

We have also performed two experiments using C furnace, at 700 and 900 °C. None display hematite. By comparison, when using the $LaCrO_3$ furnace at 700 °C and otherwise identical conditions hematite is observed. As discussed by Merkulova et al. (2017), the use of a graphite furnace in their experiments buffers the oxygen fugacity at ΔQFM-2, thus inhibiting the formation of hematite. The multi-anvil assembly used here is fired at 1000 °C prior to loading the capsule, so it should be relatively dry, thus limiting H_2 diffusion from the outer part of the assembly towards the sample. However, we should not discard the possibility that graphite diffuses from the furnace into the capsule, leading to the reduction of the sample through the reaction below as evidenced in piston-cylinder assemblies (see Matjuschkin et al., 2015):

$$2\ Fe_2O_3\ sample + C = 4\ FeO\ sample + CO_2 \quad (7)$$

This reaction might explain why the use of a graphite furnace inhibits the formation of hematite either during long or short duration experiments. It also suggests that destabilization of magnetite can occur prematurely. Thermodynamic modelling indicates that magnetite is stable upon dehydration of antigorite (Piccoli et al., 2019), in agreement with the observation in nature of magnetite in partially dehydrated serpentinite in the Alps (Debret et al., 2014) or in Cerro del Almirez (Debret et al., 2015). In our case, magnetite is stable up to 800 °C, probably controlled by the stability of chlorite.

ii- Effect of the capsule material

We examined the effect of the capsule material, by performing some experiments using Au in addition to those in $Au_{80}Pd_{20}$ (see Table 2). The oxygen fugacity prevailing within the capsule can be affected by the choice of the metal due to the different permeability to H_2 and solubility of Fe as a function of the composition of the metal. The implications are two-fold: first, if H_2 is lost by diffusion, excess oxygen will remain in the capsule, see reaction (8). Also, if iron is dissolved into the metal of the capsule, excess oxygen will be released in the sample, raising its oxygen fugacity see reaction (9):

$$H_2O = H_2 + ½\ O_2 \quad (8)$$

$$FeO_{sample} = Fe_{alloy} + ½\ O_2 \quad (9)$$

Since diffusion is a thermally activated process, we should expect that increasing temperature should enhance H_2 or Fe loss to the capsule, both leading to more oxidation of the sample. We observe that hematite coexists most of the time with chlorite, and is absent in the highest-temperature experiments, thus meaning that it is a low temperature phase. Thus, we cannot explain hematite formation due to an experimental artefact leading to the opening of the system. Also, by comparing two samples synthesized in the same experiment but in different capsule material (#900A and #900B at 800°C) we observe hematite in both capsules, and similar X_{Mg} in olivine and orthopyroxene, therefore similar oxygen fugacity.

In addition, the measured profiles of Fe diffusion into $Au_{80}Pd_{20}$ or Au capsules evidence that a similar amount of iron is dissolved into both capsule materials (see Supplementary Figure 3). Thus, both capsule materials seem to provide similar conditions to the samples.

iii- Effect of heating duration

Our experiments are very short (5 to 24 hours), especially in comparison to those of Merkulova et al. (2016) which lasted up to 9 days. In the more recent study of Iacovino et al. (2020), where experiments were performed at 800 °C, oxygen fugacity reaches stable values after 5 hours of heating. In order to verify if equilibrium was reached in our samples, we performed experiments as a function of heating duration. Given the fine-grained texture of the dehydration products (see Figure 3), the compositional changes of antigorite breakdown are accommodated rapidly, judging from the iron partitioning between olivine and enstatite close to 1 (see above). The kinetics of the oxide re-equilibration are more problematic as this phase is not neo-formed like chlorite, olivine and orthopyroxene, it requires more time to equilibrate. However, kinetics become crucial at temperatures above 800 °C when magnetite is not stable, as dissolution into olivine and orthopyroxene is sluggish. Thus, counter-intuitively, experiments at low temperatures reach equilibrium faster than those at high temperature (above 800 °C) because magnetite is stable.

With increasing heating duration from 5h (#735) to 12h (#737) at 840 °C, magnetite had time to completely disappear and get incorporated into the silicates, and $Kd_{Fe\text{-}Mg}^{Ol/Opx}$ converges to the equilibrium value around 1.0. This was the case in the second series of experiments with an olivine trap. After heating at 24 hours at 800 °C, olivine and orthopyroxene have the same composition after for 12 hours of annealing (#831 and #827).

iv-Powder versus cored samples and effect of extra olivine trap

To test whether equilibrium was attained in the experiments using cylinders, we also used powdered samples. As shown in Table 2 and in Figure 6, we observe no significant difference between the first series of experiments where serpentinite cylinder was used and the second and third series of experiments where powdered serpentinite was used. Especially, the presence of

hematite is observed in both cored and powdered samples. This can be explained by the fact that after antigorite breakdown a similar grain size is achieved in both types of experiments, thus diffusion characteristic distances are similar for both types of starting materials.

As shown by samples of the second series (#737 with an olivine trap) compared to those of the second series (#827 and #832, no an olivine trap), magnetite seems to dissolve faster when in presence of the olivine trap. This suggests that the olivine trap made of Fo90 buffers the oxygen fugacity at lower values. The influence of the trap on the rest of the sample is made efficient by the saturation in fluid. The olivine trap can be considered as representative of the primary olivine that may coexist with antigorite+magnetite in a peridotite not yet fully serpentinized. As such, the first and second series of experiments, containing the olivine trap with X_{Mg} of 0.90, are more representative of processes undergoing in partially hydrated peridotite, while the third series of experiments is more representative of what happens locally in a fully serpentinized peridotite.

To conclude about the open versus closed system, it seems that in this study, the system remained closed both because of the short duration of the experiments but also because the $LaCrO_3$ furnace seems to be inert with respect to f_{O2}. We can thus consider that the samples evolved controlled by their own, intrinsic fugacity.

Comparison with previous studies

We observe similar stability of natural serpentinite as in previous experimental studies, however we do observe the formation of hematite, which was never reported before. Hematite appears at the onset of antigorite dehydration and persists until 800-850 °C, often in coexistence with antigorite and/or chlorite (see Figure 6). At 3 GPa, the oxygen fugacity of the samples increases

with increasing temperature from 3.1 to 4.1 log units above QFM in the range of 680 to 800 °C (see Figure 9). Then it seems to decrease to 3.7 at 850 °C. Higher X_{Mg} in olivine and in orthopyroxene favors high oxygen fugacities in agreement with previous reports (Nitsan, 1974). The destabilization of magnetite upon chlorite breakdown around 800 °C induces an increase of iron content in olivine and orthopyroxene, consequently causing a decrease in oxygen fugacity (see Eq. 2). Furthermore, thermodynamic modelling of Piccoli et al. (2019) predict that upon chlorite breakdown, ~800°C, the appearance of garnet should cause a stronger decrease in oxygen fugacity of 4 log units, from ΔQFM +1 to ΔQFM -3 (see also Figure 9). However, as already discussed, our starting material contains minute amounts of Ca and little Al, most of it being incorporated in orthopyroxene, causing a retardation of garnet formation.

The high oxygen fugacities observed in this study agree with the thermodynamic model of Evans and Powell (2015) between 650 and 850 °C for similar redox budgets (see Table 1). In contrast, the oxygen fugacities observed experimentally in this study are much higher than those proposed by Piccoli et al. (2019), between ΔQFM+0.5 and ΔQFM+1 between 625 and 775°C, for a model peridotite containing 12 wt.% of FeO (see Table 1 for starting compositions). In comparison, the serpentinite used in this study contains less than 8 wt.% FeO and this may be the reason for the higher oxygen fugacity values: the higher the iron content in olivine and orthopyroxene the lower the oxygen fugacity (Nitsan, 1974).

Compared to previous experimental studies of antigorite dehydration, the oxygen fugacities found here for the post-antigorite parageneses are higher, with Δlog(QFM) of +3 to +4 at 3 GPa in the temperature range of 660-850 °C than those found by Merkulova et al. (2017), Δlog(QFM) of -2 to -4 at 2 GPa and 550-700 °C. The pressure and temperature conditions are similar in both studies thus the difference in f_{O2} recorded is most likely due to experimental design. As discussed above, an important difference between both studies is the buffering of oxygen fugacity: that is buffered at QFM-2 in an open the system in the case of

Merkulova et al. (2016), while in our case the oxygen fugacities recorded are intrinsic to the serpentinite system, which remained closed.

Finally, the oxygen fugacities reported here are higher than those measured by Iacovino et al. (2020), between ΔQFM +1.5 and +2.5 at 1 GPa and 800°C using Ni_xPd_{1-x} f_{O2} sensor. For 900°C, they measure ΔQFM +2.5, which is close to that of our sample made at 850°C, i.e. ΔQFM +3.7. Note that our starting material has a higher redox budget 0,24, than that of Iacovino et al. (2020), 0,14, see Table 1.

Natural evidences for fluids with high redox budget

Reports on arc magmas indicate values of Fe^{3+}/Fe_{total} that are higher (0.18 - 0.32; Kelley and Cottrell, 2009, 2012; Gaborieau et al., 2020) than in MORBs (0.13 - 0.17, Bézos and Humler, 2005; Cottrell and Kelley, 2011; Berry et al., 2018), and which are furthermore positively correlated with water contents in melt inclusions (Kelley and Cottrell, 2009; Gaborieau et al., 2020). Estimates of the oxygen fugacity at which the melts equilibrated yields ΔQFM ~1.5 ±1 (Carmichael, 1991; Kelley and Cottrell, 2009; 2012; Brounce et al., 2014). Estimates of f_{O2} in the mantle wedge above subduction zones as inferred from the ferric/ferrous ratio of iron in spinel peridotites xenoliths (Brandon and Draper, 1996; Parkinson and Arculus, 1999; Bénard et al., 2018) and mineral assemblages in basic lavas (Carmichael, 1991) also yield values ranging from QFM+1 to QFM+2. A similar range is reported for orogenic garnet-bearing peridotites from the Sulu Belt or the Alps, thought to be representative of the metasomatized mantle wedge (Malaspina et al., 2009). Even more oxidized examples are found in subduction zone mélanges representing the slab-mantle interface, with extremely high values of oxygen fugacity ΔQFM +12 (at 1 bar, e.g., Tumiati et al., 2015).

However, the question of whether or not these evidences relate to the redox state of the source of arc magmas is still an ongoing debate. The V/Sc and Zn/Fe systematics in MOR and arc basalts display similarities, which indicate that they formed under similar conditions of oxygen fugacity near QFM (Lee at al., 2005, 2010; Mallman and O'Neill, 2005). If this is the case, then the oxidized character of arc magmas must be explained by differentiation in the crust or by degassing of sulfur (Burgisser and Scaillet, 2007). However, so far, evidences for effects of crystallization of olivine (sink of Fe^{2+}) or magnetite (sink of Fe^{3+}) on the Fe^{3+}/Fe ratios of arc glasses are lacking (Brounce et al., 2014).

In this study, we show that fluids forming due to antigorite dehydration are equilibrated at high oxygen fugacities of ΔQFM +2 to +4 (see Figure 10). To expel such highly oxidized fluids from the slab could explain the higher redox state of arc magmas compared to MORB. These fluids can communicate their redox potential either via solutes of variable valences such as sulfur or carbon (as proposed by Merkulova et al., 2017). However, these are present in small amounts in the serpentinized mantle that subducted to sub-arc conditions (Debret et al., 2014b; Alt et al., 2012). An alternative model (see reaction below) was proposed by Iacovino et al. (2020) whereby the redox potential is transferred by electrons in the fluid which can exchange infinitely with the iron- or transition-element -bearing rocks through which the fluid travels (Tumiati et al., 2015).

$$2Fe^{2+}(s) + 2\ H^{+}(aq) \leftrightarrow 2Fe^{3+}(s) + H_2(aq) \quad (10)$$

The change occurring in the physical and chemical properties of water at around 3 GPa and 600-800°C, which leads to a more ionic liquid as suggested by previous studies (e.g., Bureau and Keppler, 1999; Till et al., 2012), probably facilitates such reaction.

Of course, that the fluids can carry a high redox potential does not mean that they actually do across the entire subduction zone. Evidences that fluids do transfer a high redox potential exist in mafic high-pressure rocks representing subducting lithosphere. For example,

Philippot and Selverstone (1992) report the presence of anhydrite ($CaSO_4$) and hematite in fluid inclusions within omphacites in eclogites from the Alps, but anhydrite coexisting with pyrite seems to be common to many inclusions worldwide (Frezzotti and Ferrando, 2015). Still, the picture is probably more complicated as evidences for reduced fluids also exist in the form of CH_4 inclusions (Song et al., 2009), precipitation of graphite (Malvoisin et al., 2011; Galvez et al., 2013) or sulfide veins (Li et al., 2020).

CONCLUSIONS

By performing experiments at 3 GPa and 600 to 900 °C, we have reproduced the different stages of prograde high-pressure dehydration of natural antigorite + magnetite assemblage. The new paragenesis contains secondary antigorite, chlorite, olivine, orthopyroxene and a fluid phase. Despite difference in Al and Fe content, we find similar phase boundaries as previously reported, however, we observe the formation of hematite that was not reported before. Hematite is observed concomitantly with high X_{Mg} in olivine, of 0.94-0.97, generally at low temperatures, below 800 °C, in coexistence with chlorite. The X_{Mg} of silicates decreases at higher temperatures once chlorite is destabilized and magnetite breakdown starts. The oxygen fugacity of the samples range between 3.0 and 4.1 log units above QFM, and increase with increasing temperature in the chlorite stability field but then decrease above chlorite stability around 800°C.

We tested the effect of our experimental strategy on the phase equilibria by varying : i) furnace material (lanthanum chromite versus graphite), ii) capsule material, iii) heating duration and iv) presence of an olivine trap. We can reasonably conclude that the antigorite dehydration proceeds in our experiments in a closed system, principally because of the use of chromite

furnace that is relatively inert, and because of the short heating durations that limit the loss or gain of H_2. Especially we find that the addition of a San Carlos olivine trap (with Fo90 composition) accelerates magnetite disappearance by driving down the oxygen fugacity of the entire system thanks to an efficient fluid transport.

We thus confirm that serpentine dehydration releases fluids equilibrated at a very high oxygen fugacity. Such high f_{O2} will induce sulfur oxidation into sulfate as proposed in numerical models (Debret and Sverjensky, 2017). Fluids with such an oxidizing potential have strong consequences on the mantle wedge physical and chemical properties (through $SO_4^{2-}{}_{(aq)}$ transport or electron transport) and consequently on the oxidation state of the source of arc magmas. The oxidizing character of the antigorite breakdown reaction and of the associated fluids could thus be a relevant explanation of the high oxidation state of arc magmas compared to MORBs (Kelley and Cottrell, 2009; Gaborieau et al., 2020).

Acknowledgements

We thank D. Mainprice for providing the natural sample of serpentinite which was used as starting material. We are grateful to Kayla Iacovino and an anonymous reviewer for their very constructive comments. We warmly thank José-Alberto Padrón-Navarta for guidance in the thermodynamic calculations as well as in many other aspects. Denis Andrault also for his insight into our f_{O2} calculations. This work was financed by the ANR HYDEEP "Hydrogen in the Deep Earth" project to N. Bolfan-Casanova and the ANR OxyDeep project to Denis Andrault. We also thank J.-L. Devidal, for his assistance during microprobe analysis; J.-M. Hénot for assistance with the SEM; J.-L. Fruquière and C. Guillot for machining the multi-anvil parts; Claire Fonquernie for measuring the volatiles content using the elemental analyzer. This is Laboratory of Excellence Clervolc contribution number xxx.

REFERENCES

Alt, J.C., Schwarzenbach, E.M., Früh-Green, G.L., Shanks, W.C., Bernasconi, S.M., Garrido, C.J., Crispini, L., Gaggero, L., Padrón-Navarta, J.A., Marchesi, C., 2013. The role of serpentinites in cycling of carbon and sulfur: Seafloor serpentinization and subduction metamorphism. Lithos 178, 40–54. doi:10.1016/J.LITHOS.2012.12.006

Andreani, M., Daniel, I., Pollet-Villard, M., 2013. Aluminum speeds up the hydrothermal alteration of olivine. American Mineralogist 98, 1738–1744.

Bean, V.E., Akimoto, S., Bell, P.M., Block, S., Holzapfel, W.B., Manghnani, M.H., Nicol, M.F., Stishov, S.M., 1986. Another step toward an international practical pressure scale. Phys. B+C 139–140, 52–54. doi:10.1016/0378-4363(86)90521-8

Benard, A., Woodland, A. B., Arculus, R. J., Nebel, O. & McAlpine, S. R. B. Variation in sub-arc mantle oxygen fugacity during partial melting recorded in refractory peridotite xenoliths from the West Bismarck Arc. *Chem. Geol.* **486**, 16-30, doi:10.1016/j.chemgeo.2018.03.004 (2018).

Berry, A. J., Stewart, G. A., O'Neill, H. S. C., Mallmann, G., & Mosselmans, J. F. W. (2018). 825 A re-assessment of the oxidation state of iron in MORB glasses. Earth and Planetary 826 Science Letters, 483, 114-123. https://doi.org/10.1016/j.epsl.2017.11.032

Bézos, A., Humler, E., 2005. The $Fe^{3+}/\Sigma Fe$ ratios of MORB glasses and their implications for mantle melting. Geochim. Cosmochim. Acta 69, 711–725. doi:10.1016/j.gca.2004.07.026.

Bose, K., Navrotsky, A., 1998. Thermochemistry and phase equilibria of hydrous phases in the system MgO-SiO2-H2O: Implications for volatile transport to the mantle. J. Geophys. Res. 103, 9713. doi:10.1029/98JB00506.

Bliss N.W. and MacLean W.H., 1975, The paragenesis of zoned chromite from central Manitoba, Geochem. Cosmochim. Acta 39: 973-990.

Bureau, H. & Keppler, H. Complete miscibility between silicate melts and hydrous fluids in the upper mantle: experimental evidence and geochemical implications. *Earth Planet. Sci. Lett.* **165**, 187-196, doi:10.1016/s0012-821x(98)00266-0 (1999).

Burkhard D. 1993, Accessory chromium spinels: Their coexistence and alteration in serpentinites, Geoch. Cosmoch. Acta 37:1297406.

Burgisser, A. & Scaillet, B. Redox evolution of a degassing magma rising to the surface. *Nature* **445**, 194-197, doi:10.1038/nature05509 (2007).

Brandon, A.D., Draper, D.S., 1996. Constraints on the origin of the oxidation state of mantle overlying subduction zones: An example from Simcoe, Washington, USA. Geochim. Cosmochim. Acta 60, 1739–1749. doi:10.1016/0016-7037(96)00056-7

Brey, G.P., Köhler, T., 1990. Geothermobarometry in Four-phase Lherzolites II. New Thermobarometers, and Practical Assessment of Existing Thermobarometers. J. Petrol. 31, 1353–1378. doi:10.1093/petrology/31.6.1353

Bromiley, G.D., Pawley, A.R., 2003. The stability of antigorite in the systems MgO-SiO2-H2O (MSH) and MgO-Al2O3-SiO2-H2O (MASH): The effects of Al3+substitution on high-pressure stability. Am. Mineral. 88, 99–108. doi:10.2138/am-2003-0113

Brounce, M. N., Kelley, K. A. & Cottrell, E. Variations in Fe3+/Sigma Fe of Mariana Arc Basalts and Mantle Wedge fO(2). *J. Petrol.* **55**, 2513-2536, doi:10.1093/petrology/egu065 (2014).

Cannat, M., Bideau, D., Hébert, R., 1990. Plastic deformation and magmatic impregnation in serpentinized ultramafic rocks from the Garrett transform fault (East Pacific Rise). Earth Planet. Sci. Lett. 101, 216–232. doi:10.1016/0012-821X(90)90155-Q

Capitani G, Mellini M (2004) The modulated crystal structure of antigorite: the m = 17 polysome. Am Mineral 89:147–158.

Carmichael, I.S.E., 1991. The redox states of basic and silicic magmas: a reflection of their source regions? Contrib. to Mineral. Petrol. 106, 129–141. doi:10.1007/BF00306429

Cottrell, E., Kelley, K.A., 2011. The oxidation state of Fe in MORB glasses and the oxygen fugacity of the upper mantle. Earth Planet. Sci. Lett. 305, 270–282. doi:10.1016/j.epsl.2011.03.014

de Faria, D.L.A., Venâncio Silva, S., de Oliveira, M.T., 1997. Raman micro spectroscopy of some iron oxides and oxyhydroxides. J. Raman Spectrosc. 28, 873–878. doi:10.1002/(SICI)1097-4555(199711)28:11<873::AID-JRS177>3.0.CO;2-B

Debret, B., Andreani, M., Muñoz, M., Bolfan-Casanova, N., Carlut, J., Nicollet, C., Schwartz, S., Trcera, N., 2014a. Evolution of Fe redox state in serpentine during subduction. Earth Planet. Sci. Lett. 400, 206–218. doi:10.1016/j.epsl.2014.05.038

Debret, B., Bolfan-Casanova, N., Padrón-Navarta, J.A., Martin-Hernandez, F., Andreani, M., Garrido, C.J., López Sánchez-Vizcaíno, V., Gómez-Pugnaire, M.T., Muñoz, M., Trcera, N., 2015. Redox state of iron during high-pressure serpentinite dehydration. Contrib. to Mineral. Petrol. 169, 36. doi:10.1007/s00410-015-1130-y

Debret, B., Millet, M.-A., Pons, M.-L., Bouilhol, P., Inglis, E., Williams, H., 2016. Isotopic evidence for iron mobility during subduction. Geology 44, 215–218. doi:10.1130/G37565.1

Debret, B., Sverjensky, D.A., 2017. Highly oxidising fluids generated during serpentinite breakdown in subduction zones. Sci. Rep. 7, 10351. doi:10.1038/s41598-017-09626-y

Deschamps, F., Guillot, S., Godard, M., Chauvel, C., Andreani, M., Hattori, K., 2010. In situ characterization of serpentinites from forearc mantle wedges: Timing of serpentinization and behavior of fluid-mobile elements in subduction zones. Chem. Geol. 269, 262–277.

doi:10.1016/j.chemgeo.2009.10.002

Evans, B., Johannes, W., Oterdoom, H., Trommsdorff, V., 1976. Stability of crystotile and serpentinite in the serpentine multisystem. Schweiz. Mineral. Petrogr. Mitt. 56, 79-93.

Evans, B.W., Trommsdorff, V., 1978. Petrogenesis of garnet lherzolite, Cima di Gagnone, Lepontine Alps. Earth Planet. Sci. Lett. 40, 333–348. doi:10.1016/0012-821X(78)90158-9

Evans, K.A., 2006. Redox decoupling and redox budgets: Conceptual tools for the study of earth systems. Geology 34, 489-492.

Evans, K.A., 2012. The redox budget of subduction zones. Earth-Science Rev. 113, 11–32. doi:10.1016/j.earscirev.2012.03.003

Evans, K.A., Tomkins, A.G., 2011. The relationship between subduction zone redox budget and arc magma fertility. Earth Planet. Sci. Lett. 308, 401-409.

Evans, K.A., Reddy, S.M., Tomkins, A.G., Crossley, R.J., Frost, B.R., 2017. Effects of geodynamic setting on the redox state of fluids released by subducted mantle lithosphere. Lithos, 278-281, 26–42.

Evans, K.A., Powell, R., 2015. The effect of subduction on the sulphur, carbon and redox budget of lithospheric mantle. J. Metamorph. Geol. 33, 649-670.

Frezzotti, M. L. & Ferrando, S. The chemical behavior of fluids released during deep subduction based on fluid inclusions. *Am. Miner.* **100**, 352-377, doi:10.2138/am-2015-4933 (2015).

Fumagalli, P., Poli, S., 2005. Experimentally Determined Phase Relations in Hydrous Peridotites to 6.5 GPa and their Consequences on the Dynamics of Subduction Zones. J. Petrol. 46, 555–578.

Gaetani, G.A., Grove, T.L., 1998. The influence of water on melting of mantle peridotite. Contrib. to Mineral. Petrol. 131, 323–346. doi:10.1007/s004100050396

Garrido, C.J., López Sánchez-Vizcaíno, V., Gómez-Pugnaire, M.T., Trommsdorff, V., Alard, O., Bodinier, J.-L., Godard, M., 2005. Enrichment of HFSE in chlorite-harzburgite produced by high-pressure dehydration of antigorite-serpentinite: Implications for subduction magmatism. Geochemistry, Geophys. Geosystems 6, n/a-n/a. doi:10.1029/2004GC000791

Gasparik, T., 2003. Phase Diagrams for Geoscientists: An Atlas of the Earth's Interior.

Gaborieau M., Laubier M., Bolfan-Casanova N., McCammon C.A., Vantelon D., Chumakov A.I., Schiavi F., Neuville D.R., Venugopal S., 2020, Determination of $Fe^{3+}/\Sigma Fe$ of olivine-hosted melt inclusions using Mössbauer and XANES spectroscopy, accepted at Chemical Geology.

Gervilla, F., Padrón-Navarta, J.A., Kerestedjian, T., Sergeeva, I., González-Jiménez, J.M., Fanlo, I., 2012. Formation of ferrian chromite in podiform chromitites from the Golyamo Kamenyane serpentinite, Eastern Rhodopes, SE Bulgaria: A two-stage process. Contrib. Mineral. Petrol. 164, 643-657.

Grove, T.L., Chatterjee, N., Parman, S.W., Médard, E., 2006. The influence of H_2O on mantle wedge melting. Earth Planet. Sci. Lett. 249, 74–89. doi:http://dx.doi.org/10.1016/j.epsl.2006.06.043

Guillot, S., Hattori, K.H., de Sigoyer, J., 2000. Mantle wedge serpentinization and exhumation of eclogites: Insights from eastern Ladakh, northwest Himalaya. Geology 28, 199. doi:10.1130/0091-7613(2000)28<199:MWSAEO>2.0.CO;2

Guillot, S., Schwartz, S., Reynard, B., Agard, P., Prigent, C., 2015. Tectonic significance of serpentinites. Tectonophysics 646, 1–19.

Hernlund, J., Leinenweber, K., Locke, D., Tyburczy, J. A., 2006. A numerical model for steady-state temperature distributions in solid-medium high-pressure cell assemblies. American Mineralogist 91, 295–305.

Holland, T. J. B., Powell, R., Sciences, E. & Cb, C., 1998, An internally consistent thermodynamic data set for phases of petrological interest. *J. Metamorph. Geol.* **16**, 309–343.

Kelley, K.A., Cottrell, E., 2012. The influence of magmatic differentiation on the oxidation state of Fe in a basaltic arc magma. Earth Planet. Sci. Lett. 329–330, 109–121. doi:10.1016/j.epsl.2012.02.010

Kelley, K.A., Cottrell, E., 2009. Water and the oxidation state of subduction zone magmas. Science 325, 605–607. doi:10.1126/science.1174156

Klein, F., Bach, W., Humphris, S.E., Kahl, W.A., Jons, N., Moskowitz, B., Berquo, T.S., 2014. Magnetite in seafloor serpentinite--Some like it hot. Geology 42, 135–138.

Klein, F., Marschall, H.R., Bowring, S.A., Humphris, S.E., Horning, G., 2017. Mid-ocean Ridge Serpentinite in the Puerto Rico Trench: from Seafloor Spreading to Subduction. Journal of Petrology 58, 1729–1754.

Lee, C. T. A., Leeman, W. P., Canil, D., & Li, Z. X. A. (2005). Similar V/Sc systematics in 935 MORB and arc basalts: Implications for the oxygen fugacities of their mantle source 936 regions. Journal of Petrology, 46(11), 2313-2336. https://doi.org/10.1093/petrology/egi056 937

Lee, C. T. A., Luffi, P., Le Roux, V., Dasgupta, R., Albaréde, F., & Leeman, W. P. (2010). The 938 redox state of arc mantle using Zn/Fe systematics. Nature, 468, 681-685. 939 https://doi.org/10.1038/nature09617

Li, J.-L. *et al.* Uncovering and quantifying the subduction zone sulfur cycle from the slab perspective. *Nat. Commun.* **11**, 514, doi:10.1038/s41467-019-14110-4 (2020).

López Sánchez-Vizcaíno, V., Trommsdorff, V., Gómez-Pugnaire, M.T., Garrido, C.J., Müntener, O., Connolly, J.A.D., 2005. Petrology of titanian clinohumite and olivine at the high-pressure breakdown of antigorite serpentinite to chlorite harzburgite (Almirez Massif, S. Spain). Contrib.

to Mineral. Petrol. 149, 627–646. doi:10.1007/s00410-005-0678-3

Malvoisin, B., Carlut, J., Brunet, F., 2012. Serpentinization of oceanic peridotites: 1. A high-sensitivity method to monitor magnetite production in hydrothermal experiments. J. Geophys. Res. 117, B01104.

Marcaillou, C., Munoz, M., Vidal, O., Parra, T., Harfouche, M., 2011. Mineralogical evidence for H2 degassing during serpentinization at 300°C/300bar. Earth and Planetary Science Letters 303, 281–290.

Maurice, J., Bolfan-Casanova, N., Padrón-Navarta, J.A., Manthilake, G., Hammouda, T., Hénot, J.M., Andrault, D., 2018. The stability of hydrous phases beyond antigorite breakdown for a magnetite-bearing natural serpentinite between 6.5 and 11 GPa. Contrib. to Mineral. Petrol. 173, 86. doi:10.1007/s00410-018-1507-9.

Mellini, M., Trommsdorff, V., Compagnoni, R., 1987. Antigorite polysomatism - behavior during progressive metamorphism. Contrib. Mineral. Petrol. 97, 147-155.

Merkulova, M., Muñoz, M., Vidal, O., Brunet, F., 2016. Role of iron content on serpentinite dehydration depth in subduction zones: Experiments and thermodynamic modeling. doi:10.1016/j.lithos.2016.09.007

Merkulova, M.V., Muñoz, M., Brunet, F., Vidal, O., Hattori, K., Vantelon, D., Trcera, N., Huthwelker, T., 2017. Experimental insight into redox transfer by iron- and sulfur-bearing serpentinite dehydration in subduction zones. Earth Planet. Sci. Lett. 479, 133–143. doi:10.1016/J.EPSL.2017.09.009

Mével, C., 2003. Serpentinization of abyssal peridotites at mid-ocean ridges. Comptes Rendus Geoscience 335, 825–852.

Morten, L. and Puga, E., 1984. Blades of olivines and ortho- dissolved lithium in the oceans. Geochim.

Cosmochim. pyroxenes in ultramafic rocks from the Cerro del Almirez, Acta, 48: 859-872. Sierra Nevada Complex, Spain: relics of quench-textured Strong, D.F. and Dostal, J., 1980. Dyna. Neues Jahrb. Miner. Monatsh. 5:211-218.

Niida, K., Green, D.H., 1999. Stability and chemical composition of pargasitic amphibole in MORB pyrolite under upper mantle conditions. Contrib. to Mineral. Petrol. 135, 18–40. doi:10.1007/s004100050495

Nitsan, U. Stability field of olivine qwith respect to oxidation and reduction. *Journal of Geophysical Research* **79**, 706-711, doi:10.1029/JB079i005p00706 (1974).

O'Neill Hugh StC, The quartz-fayalite-iron and quartz-fayalite-magnetite equilibria and the free energies of formation of fayalite (Fe_2SiO_4) and magnetite (Fe_3O_4), 1987, Am Mineral 72:67.-7

Oufi, O., Cannat, M., Horen, H., 2002. Magnetic properties of variably serpentinized abyssal peridotites. J. Geophys. Res. 107, 381.

Padrón-Navarta, J.A., Hermann, J., Garrido, C.J., López Sánchez-Vizcaíno, V., Gómez-Pugnaire, M.T., 2010a. An experimental investigation of antigorite dehydration in natural silica-enriched serpentinite. Contrib. to Mineral. Petrol. 159, 25–42. doi:10.1007/s00410-009-0414-5

Padrón-Navarta, J.A., Lopez Sanchez-Vizcaino, V., Garrido, C.J., Gomez-Pugnaire, M.T., 2011. Metamorphic Record of High-pressure Dehydration of Antigorite Serpentinite to Chlorite Harzburgite in a Subduction Setting (Cerro del Almirez, Nevado-Filabride Complex, Southern Spain). J. Petrol. 52, 2047–2078. doi:10.1093/petrology/egr039

Padrón-Navarta, J.A., López Sánchez-Vizcaíno, V., Garrido, C.J., Gómez-Pugnaire, M.T., Jabaloy, A., Capitani, G.C., Mellini, M. Highly ordered antigorite from Cerro del Almirez HP-HT serpentinites, SE Spain (2008) Contributions to Mineralogy and Petrology, 156 (5), pp. 679-688.

Padrón-Navarta, J.A., Tommasi, A., Garrido, C.J., Sanchez-Vizcaino, V.L., Gomez-Pugnaire, M.T.,

Jabaloy, A., Vauchez, A., 2010b. Fluid transfer into the wedge controlled by high-pressure hydrofracturing in the cold top-slab mantle. Earth Planet. Sci. Lett. 297, 271–286. doi:10.1016/j.epsl.2010.06.029

Padrón-Navarta JA, Sánchez-Vizcaíno VL, Hermann J, Connolly JAD, Garrido CJ, Gómez-Pugnaire MT, Marchesi C (2013) Tschermak's substitution in antigorite and consequences for phase relations and water liberation in high-grade serpentinites. Lithos 178:186–196

Parkinson, I.J., Arculus, R.J., 1999. The redox state of subduction zones: insights from arc-peridotites. Chem. Geol. 160, 409–423. doi:10.1016/S0009-2541(99)00110-2

Philippot, P. & Selverstone, J. Trace-element-rich brines in eclogitic veins – Implications for fluid composition and transport during subduction, 1991, *Contrib. Mineral. Petrol.* **106**, 417-430, doi:10.1007/bf00321985.

Plank, T., Langmuir, C.H., 1998. The chemical composition of subducting sediment and its consequences for the crust and mantle. Chem. Geol. 145, 325–394.

Ranero, C.R., Morgan, J.P., McIntosh, K., Reichert, C., 2003. Bending-related faulting and mantle serpentinization at the Middle America trench. Nature 425, 367–373.

Reynard, B., 2013. Serpentine in active subduction zones. Lithos, 178, 171-185.

Scambelluri M., Pettke T., Rampone E. Godard M, Reusser E. 2014. Petrology and trace element budgets of high-pressure peridotites indicate subduction dehydration of serpentinized mantle (Cima di Gagnone, Central Alps, Switzerland). Journal of Petrology, 55, 459-498.

Schmidt MW, Poli S. 2014. Devolatization during subduction. In: Rudnick RL (ed) The crust. Treatise on geochemistry, 2nd edn. Elsevier, Amsterdam, pp 669–70

Schwartz, S., Guillot, S., Reynard, B., Lafay, R., Debret, B., Nicollet, C., Lanari, P., Auzende, A.L., 2013. Pressure–temperature estimates of the lizardite/antigorite transition in high pressure

serpentinites. Lithos 178, 197–210. doi:10.1016/j.lithos.2012.11.023

Song, S., Su, L., Niu, Y., Lai, Y., Zhang, L., 2009. CH4 inclusions in orogenic harzbur- gite: evidence for reduced slab fluids and implication for redox melting in man-tle wedge. Geochim. Cosmochim. Acta73, 1737–1754.

Stagno, V. & Frost, D. J. Carbon speciation in the asthenosphere: Experimental measurements of the redox conditions at which carbonate-bearing melts coexist with graphite or diamond in peridotite assemblages. *Earth Planet. Sci. Lett.* **300**, 72-84, doi:10.1016/j.epsl.2010.09.038 (2010).

Susaki J, Akaogi M, Akimoto S, Shimomura O., 1985, Garnet-perovskite transition in CaGeO3: in situ X-ray measurements using synchrotron radiation. Geophys Res Lett 12:729–732.

Tastumi, Y. Migration of fluid phases and genesis of basalt magmas in subduction zones. *Journal of Geophysical Research*, 4697-4707. (1989).

Taylor, W.R., Green, D.H., 1988. Measurement of reduced peridotite-C-O-H solidus and implicationsfor redox melting of the mantle. Nature 332, 349–352. doi:10.1038/332349a0.

Till, C. B., Grove, T. L. & Withers, A. C. The beginnings of hydrous mantle wedge melting. *Contrib. Mineral. Petrol.* **163**, 669-688, doi:10.1007/s00410-011-0692-6 (2012).

Trommsdorff, V., Sánchez-Vizcaíno, V.L., Gómez-Pugnaire, M.T., Müntener, O., 1998. High pressure breakdown of antigorite to spinifex-textured olivine and orthopyroxene, SE Spain. Contrib. to Mineral. Petrol. 132, 139–148. doi:10.1007/s004100050412

Ulmer, P., Trommsdorff, V., 1995. Serpentine stability to mantle depths and subduction-related magmatism. Science 268, 858–861. doi:10.1126/science.268.5212.858.

Ulmer, P, Luth, R.W., 1991. The graphite-COH equilibrium in P, T, $fO2$ space. An experimental determination to 30 kbar and 1600°C. Contrib. Mineral. Petrol., 106, 265-272

von Seckendorff, V., O'Neill, H.S.C., 1993. An experimental study of Fe-Mg partitioning between

olivine and orthopyroxene at 1173, 1273 and 1423 K and 1.6 GPa. Contrib. to Mineral. Petrol. 113, 196–207. doi:10.1007/BF00283228.

Whitney, D.L., Evans, B.W., 2009. Abbreviations for names of rock-forming minerals. American Mineralogist 95, 185–187.

Wunder, B., Schreyer, W., 1997. Antigorite: High-pressure stability in the system MgO-SiO2-H2O (MSH). Lithos 41, 213–227. doi:10.1016/S0024-4937(97)82013-0

Zhang, J., Li, B., Utsumi, W., Liebermann, R., 1996. *In situ* X-ray observations of the coesite-stishovite transition: reversed phase boundary and kinetics. Phys. Chem. Miner. 23, 1–10. doi:10.1007/BF00202987

Figure 1

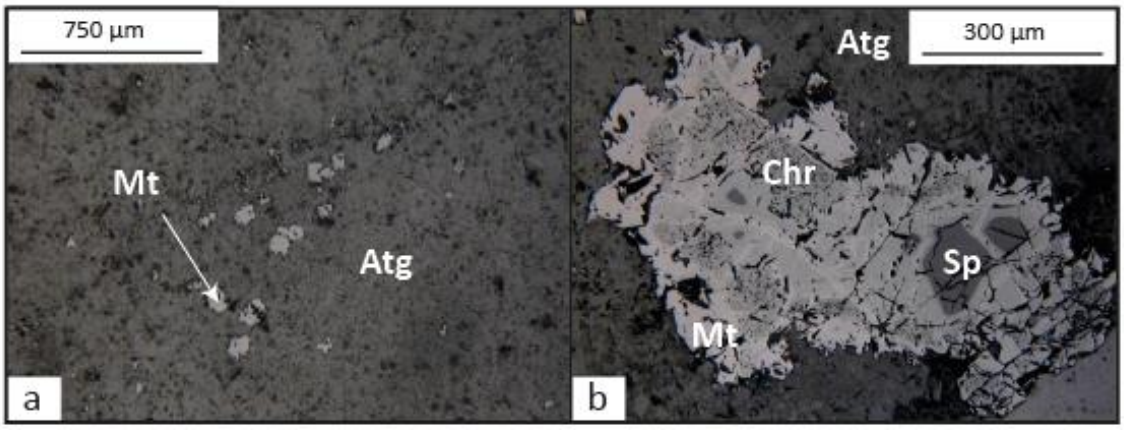

Figure 1. Microphotograph in reflective light of the serpentinite starting material from the Iron Mountain, North Cascades (Washington, USA), with (a) magnetite grains within the fine and dense antigorite matrix, and (b) composite oxides composed of Al-Cr spinel core surrounded by Al-poor, Fe-rich chromite and magnetite rims at the border.

Figure 2

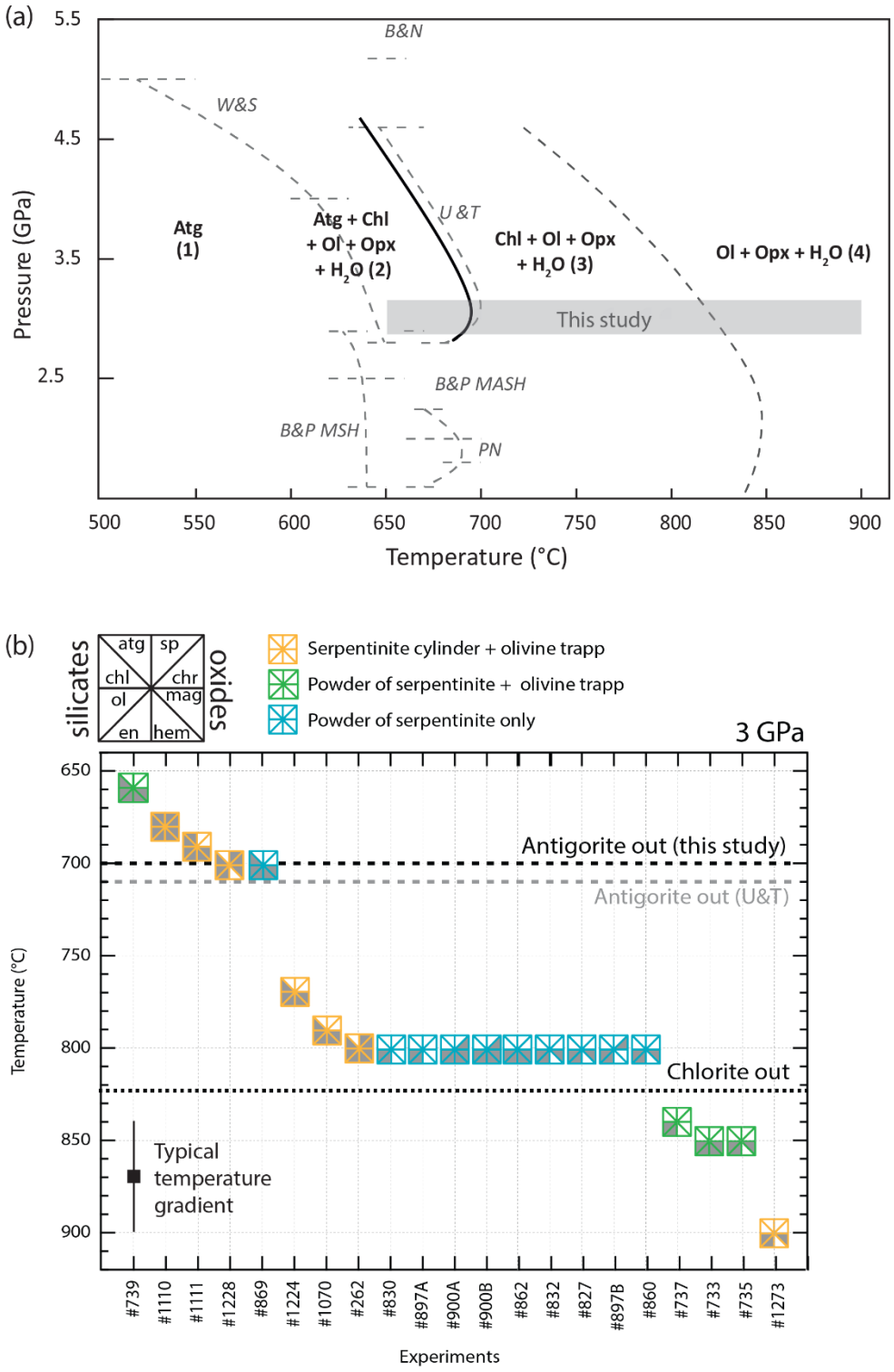

Figure 2. (a) Experimental pressure-temperature stability field of antigorite. The grey bar represents the field of investigation. Stability fields of antigorite from other experimental studies are shown as annotated dashed lines. Abbreviations are as follow; U&T: Ulmer and Trommsdorff, (1995) ; W&S: Wunder and Schreyer (1997) ; B&N: Bose and Navrotsky (1998), PN: Padrón-Navarta et al. (2010a) ; B&P: Bromiley and Pawley (2003) for both MSH and MASH systems. **(b)** Mineral paragenesis for each experiment.

Figure 3

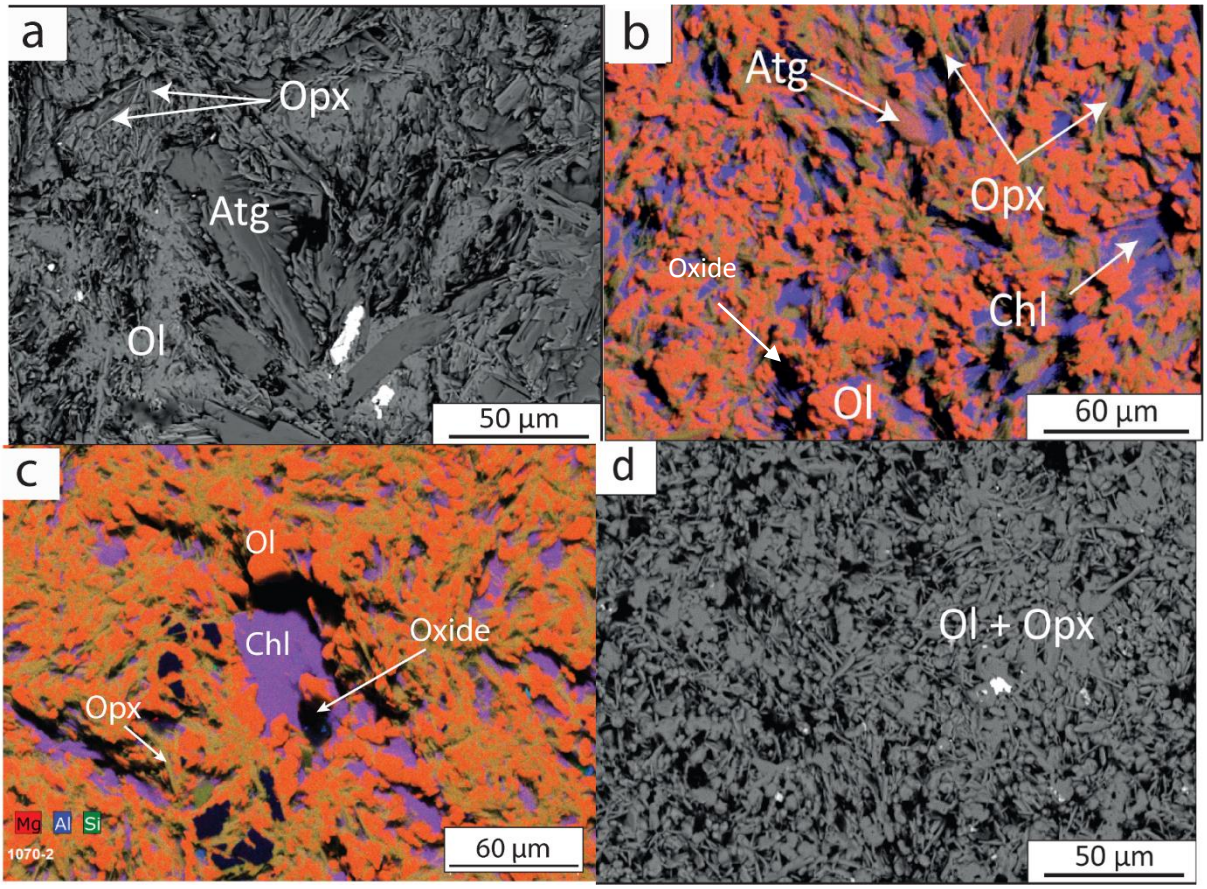

Figure 3. Scanning Electron Microscope images illustrating the characteristic microstructures of the samples after antigorite dehydration. (a) Backscatter electron scanning (BSE) image showing typical mineralogical assemblage and texture with secondary antigorite, chlorite, olivine, orthopyroxene and magnetite (#1110 synthesized at 680 °C). (b) Corresponding chemical map by Energy-dispersive X-ray spectroscopy, showing coexistence of antigorite, chlorite, olivine, orthopyroxene and an oxide. Color-coding is as follows, olivine = red-orange, chlorite = purple, antigorite = brown, and orthopyroxene = pale green dendrites, black = oxide. (c) Chemical map of sample #1070 (synthesized at 790°C) where chlorite coexists with olivine and orthopyroxene and an oxide. (d) BSE image of a sample after complete breakdown of the hydrous phases showing only olivine and orthopyroxene (#1273, 900 °C).

Figure 4

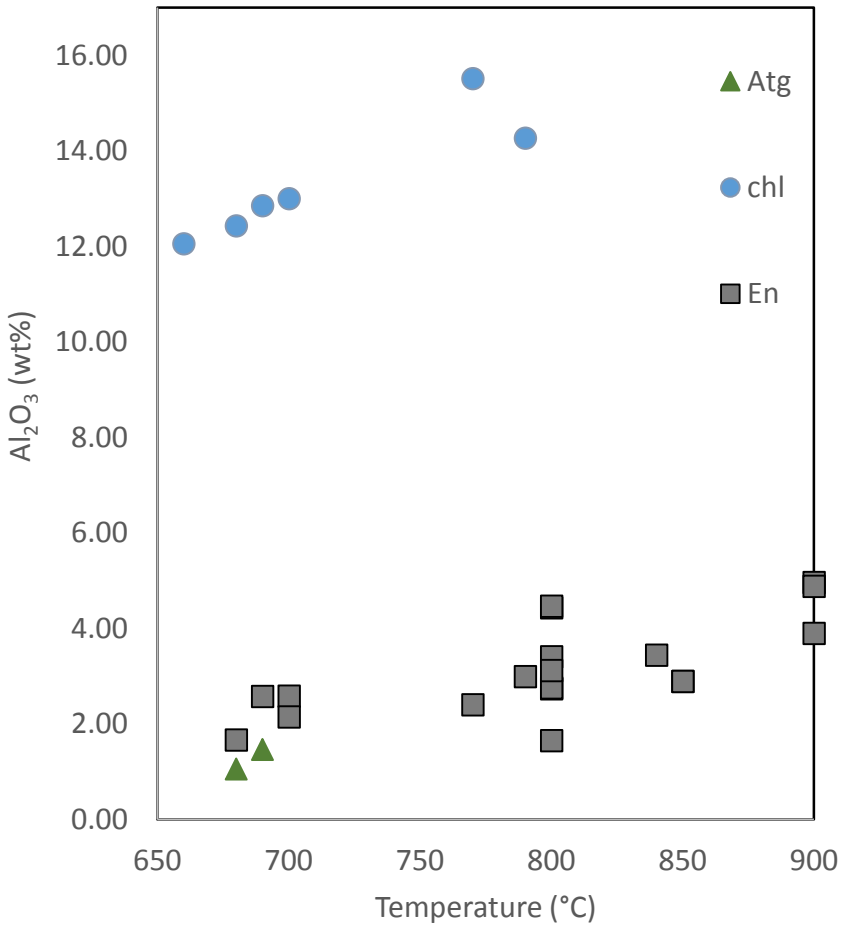

Figure 4. Evolution of concentration in Al_2O_3 wt.% in silicates (antigorite, chlorite and enstatite) as a function of experimental temperature from this study.

Figure 5

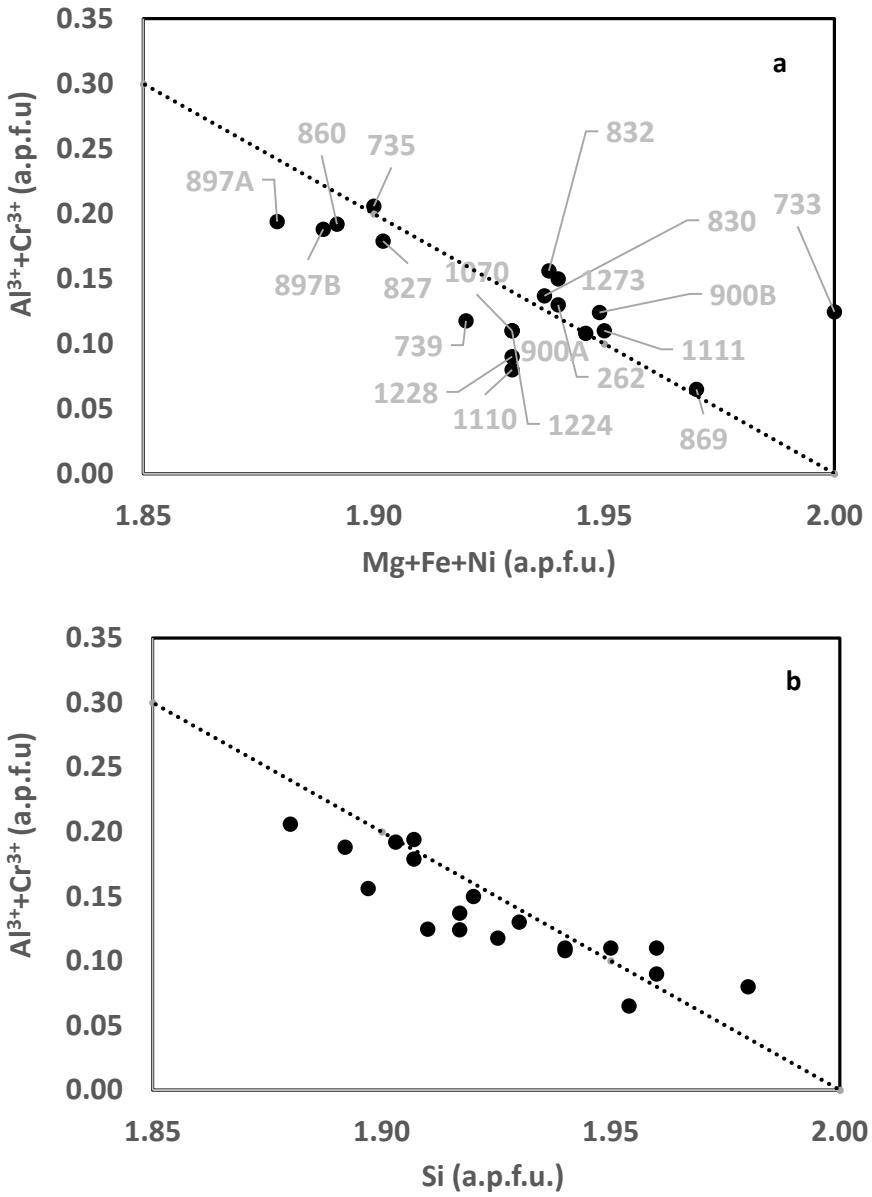

Figure 5. **(a)** Al+Cr content express in atom per formula unit (a.p.f.u.) in orthopyroxene as a function of Mg+Fe+Ni content (a.p.f.u). The grey labels refer to the experiment number (see Table 2).; **(b)** Al content (a.p.f.u.) in orthopyroxene as a function of Si content (a.p.f.u). The dashed line represents the theoretical Al Tschermak substitution in the tetrahedral site (e.g., 2 Al+Cr= Mg+Fe+Ni+Si).

Figure 6

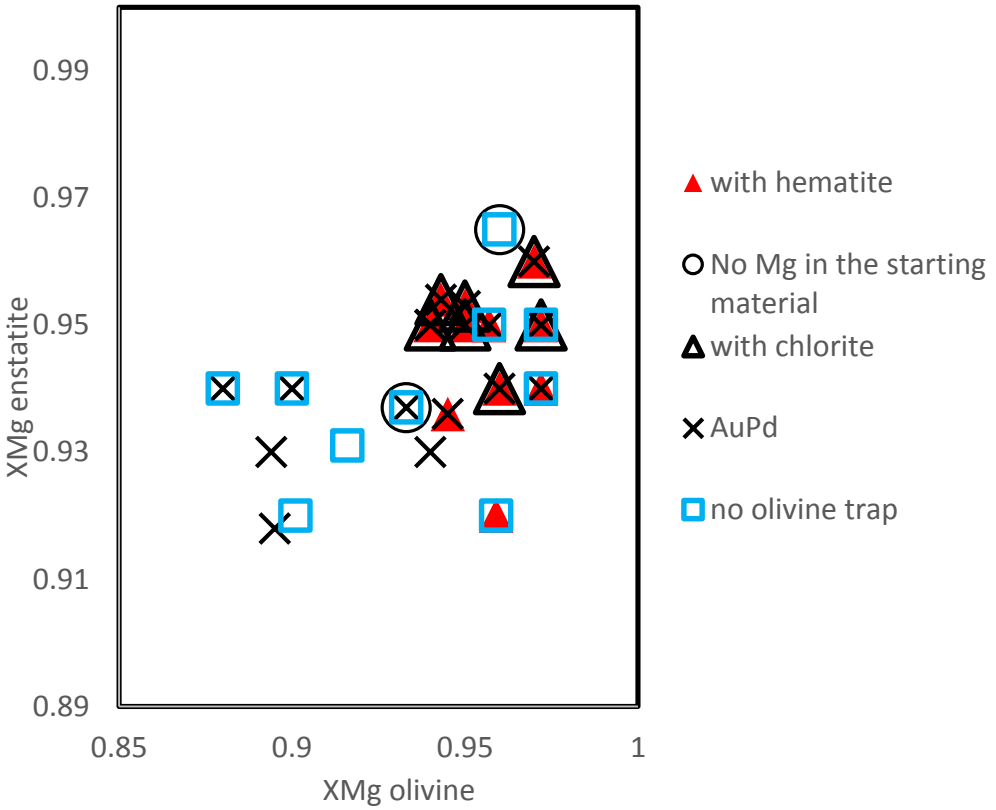

Figure 6. Dependence of X_{Mg} of enstatite on X_{Mg} of olivine and experimental conditions. The low temperature experiments are corresponding to the chlorite-bearing samples.

Figure 7

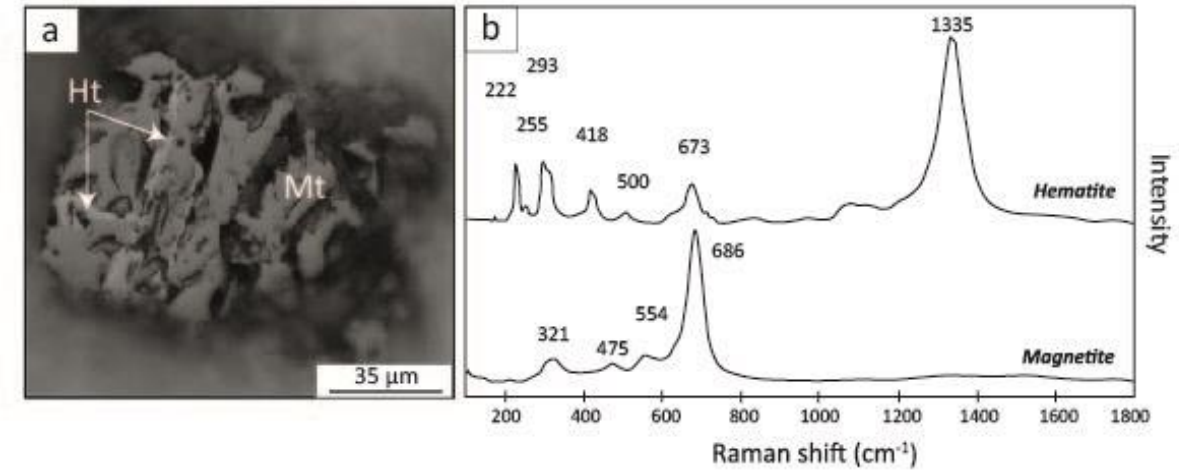

Figure 7. **(a)** Optical microscopy photograph in reflective light of a well-preserved magnetite partially transformed in hematite after antigorite dehydration, at 690 °C (#1110) ; **(b)** Corresponding Raman spectra of hematite and magnetite.

Figure 8

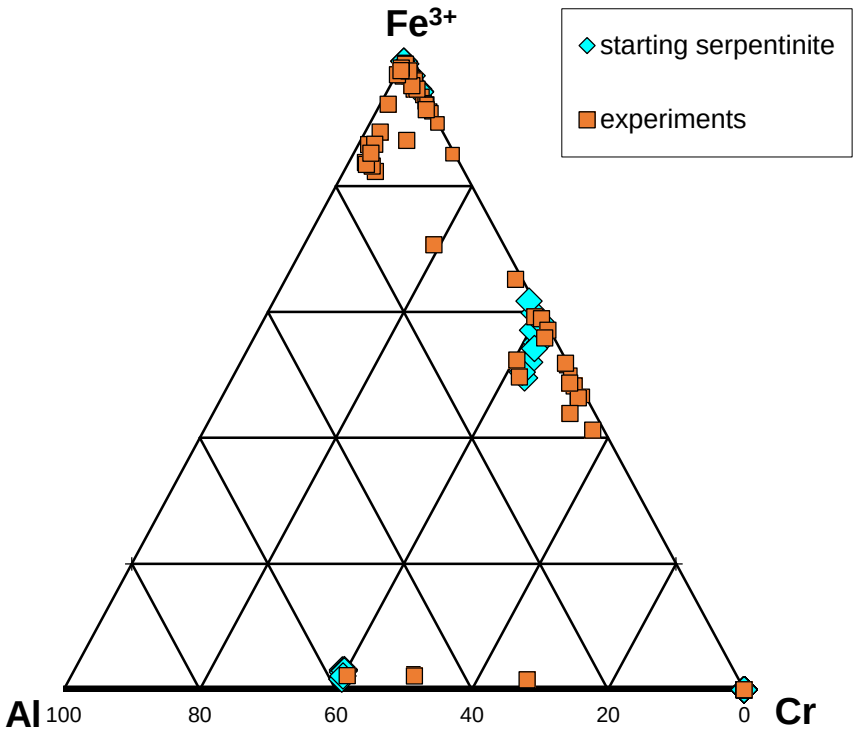

Figure 8. Ternary diagram showing the composition of the spinel oxides.

Figure 9

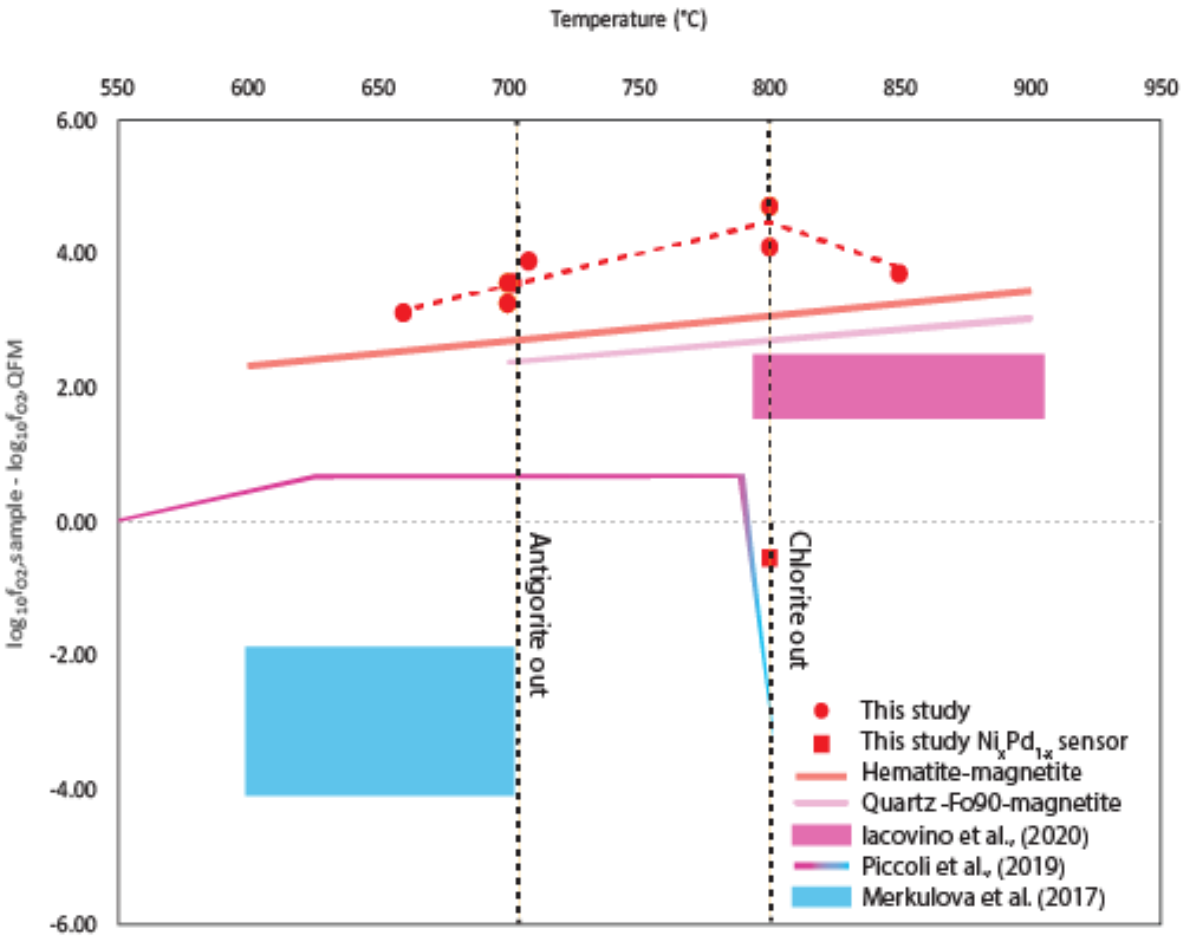

Figure 9. Oxygen fugacity relative to the Quartz-Fayalite-Magnetite (QFM) buffer of samples after antigorite dehydration, which contain hematite. Also shown is the Hematite-Magnetite (HM) equilibrium as the orange line. The Quartz-Forsterite90-Magnetite equilibrium is shown as the pink line, and was calculated assuming $X_{Mg}^{olivine} = X_{Mg}^{orthopyroxene}$. The f_{O2} reported in the experimental studies of Merkulova et al. (2017) and Iacovino et al. (2020) are shown as the blue and pink rectangles, respectively. While the thermodynamic model of Piccoli et al. (2019) is shown as the pink to blue line.

Figure 10

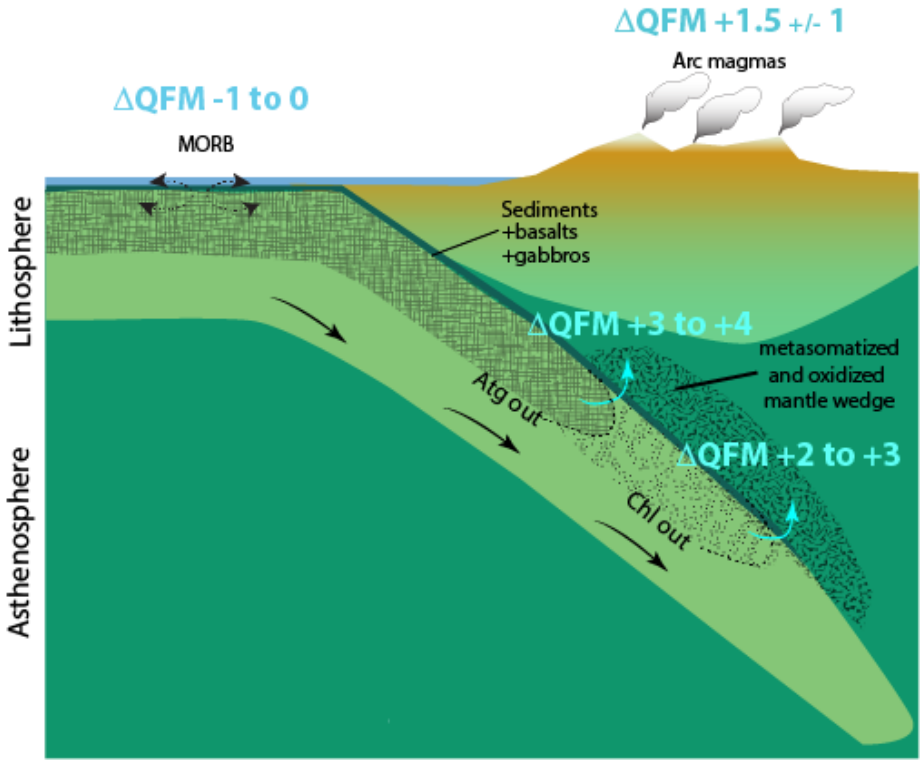

Figure 10. A model of subduction of the serpentinized mantle proposing a range of oxygen fugacity relative to the QFM buffer, for the released fluids following dehydration of antigorite and chlorite at higher pressures and temperatures. The oxygen fugacity ranges for MORB and arc magmas are from Bézos and Humler (2005), Cottrell and Kelley (2011), Berry et al. (2018) and from Kelley and Cottrell (2009, 2012), Brounce et al. (2014), Gaborieau et al. (2020), respectively.

Supplementary Figure 1a

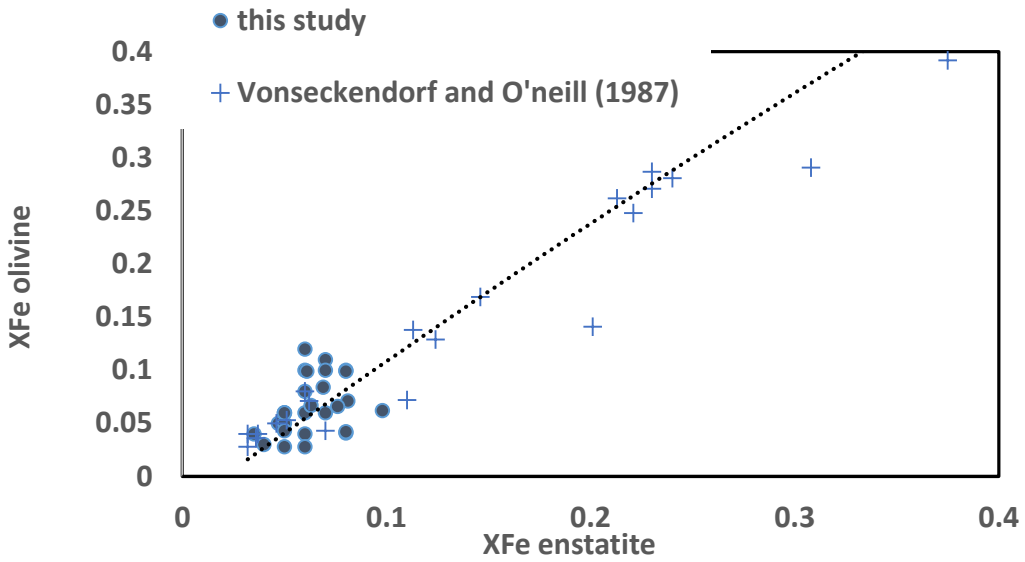

Supplementary material: Figure S1a. Evolution of X_{Fe} in enstatite as a function of X_{Fe} in olivine showing the equilibrium between both phases in comparison with the study of von Seckendorf and O'Neill (1987). Note that orthopyroxene contains significant amounts of aluminum.

Supplementary Figure 1b

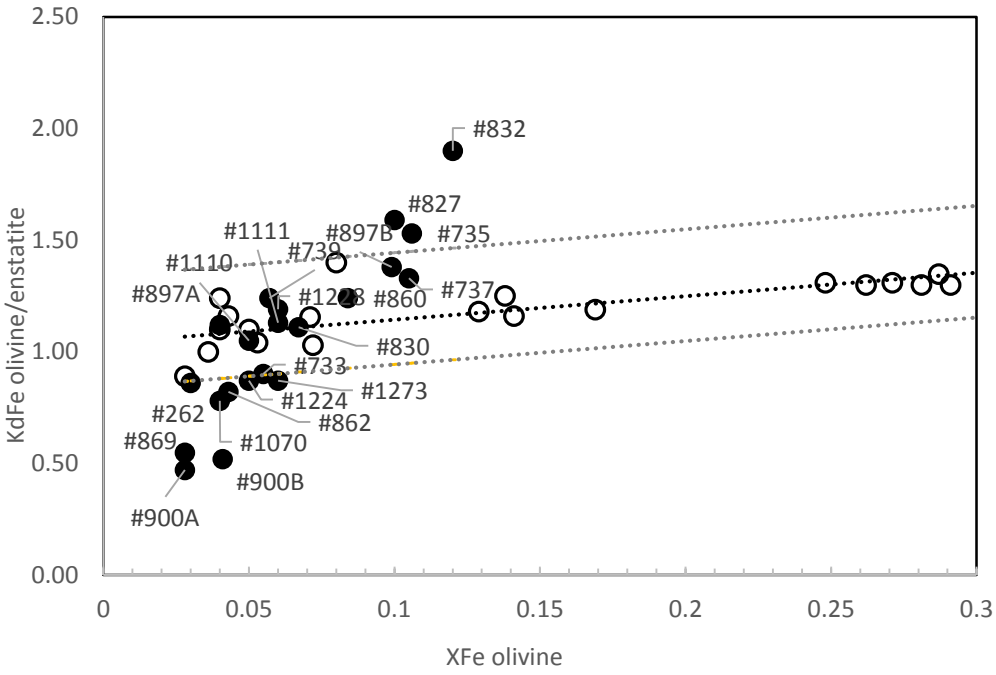

Supplementary Figure 1b. Dependence of the distribution of iron K_{Fe} between olivine and both pyroxenes as a function of the iron content in olivine X_{Fe} (full symbols: this study; empty symbols: von Seckendorf and O'Neill, 1987). A few samples from this study depart form the previous trend established experimentally by von Seckendorf and O'Neill (1987), evidencing that these samples may not have reached equilibrium. The grey dotted lines are deviations of +/- 0.2 from the trend of von Seckendorf and O'Neill (1987), which fit is shown by the black dotted line.

Supplementary Figure 2

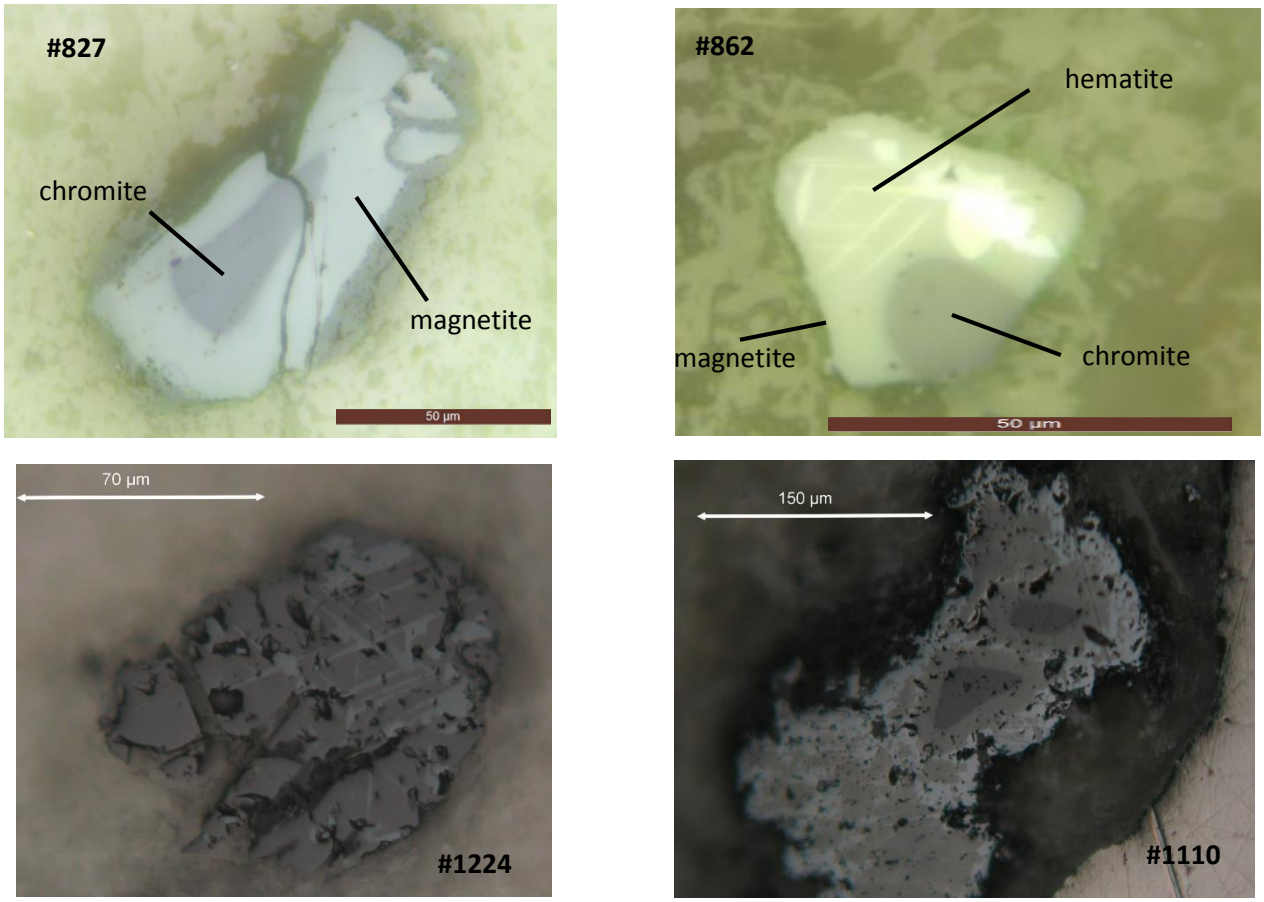

Supplementary Figure 2. Optical microphotographs in reflected light showing the diverse textures of the oxides within the serpentinite samples dehydrated at high-pressure.

Supplementary Figure 3

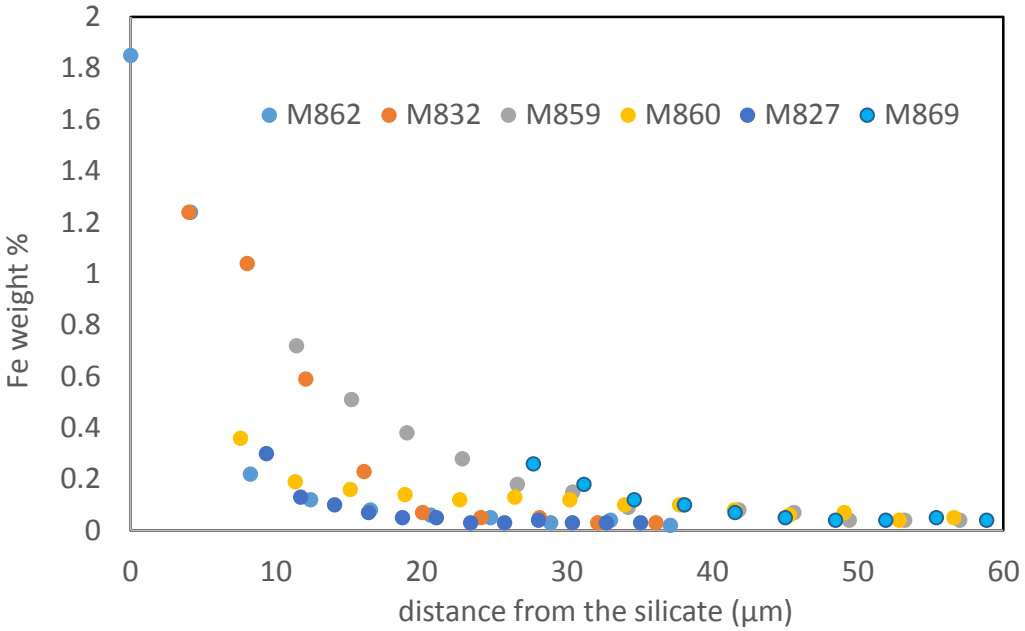

Supplementary Figure 3. Fe diffusion profile ate the edge of the sample, within the metal capsule, in wt% as measured with EPMA.

Table 1. Average bulk rock (BR) chemical composition from ICP-AES (BR1) and standard deviation (from 5 distinct batches). Bulk rock composition calculated for 94.5% antigorite and 5.5% magnetite is reported as BR2.

	Serpentinite starting mat.					Previous studies			
	BR_1		BR_2	Antigorite		Almirez (a)	Mont-Cenis Alps (b)	Voltri Alps (c)	model (d)
	ICP-AES		calc.	WDS					
SiO_2	40,04	(0,30)	40,79	43,17	(0,51)	40,34	38,02	41,54	37,1
TiO_2	0,03	(0,01)	0,04	0,03	(0,03)	0,1	0,45	0,02	-
Al_2O_3	1,63	(0,11)	1,57	1,66	(0,36)	2,81	1,92	1,44	1,89
Cr_2O_3	0,27	(0,00)	0,28	0,22	(0,08)	-	0,16	-	0,51
FeO_{Total}	7,79	(0,48)	7,48	2,60	(0,17)	6,7	6,07	7,44	11,9
FeO	3,52	-	3,57	2,00	(0,13)	2,87	1,9	4,61	-
Fe_2O_3	4,65	-	4,35	0.66[e]	(0,04)	4,26	4,8	2,54	-
NiO	0,25	(0,00)	0,15	0,16	(0,03)	-	0,04	-	-
MnO	0,09	(0,00)	0,07	0,07	(0,04)	0,09	-	0,11	-
MgO	38,94	(0,40)	36,45	38,56	(0,41)	37,48	38,52	37,43	35,5
CaO	0,02	(0,02)	0,02	0,02	(0,02)	0,07	2,43	<0,01	0,01
Total	88,64	(0,39)	87,28	86,55	(0,59)	99,5	99,11	99,56	98,5
H_2O	11.4[f]		11.39 [g]	12.05 [h]		11,47	11,5	11,5	11,5
X_{Mg}	0,90		0,90	0,96		0,91		0,90	0,84
Redox budget [i]	0.25					0.23	0.25	0.14	

[a] Padrón-Navarta et al. (2011)

[b] Merkulova et al. (2016)

[c] Iacovino et al. (2020)

[d] Piccoli et al. (2019)

[e] Fe_2O_3 estimated from $\sum Fe^{3+}/Fe_{total}$ of 0.23 (similar to sample IM3, Evans et al., 2012)

[f] H_2O content calculated from loss on ignition

[g] H_2O content estimated from modal amount of antigorite in BR

[h] H_2O content from structural formula

[i] The redox budget is calculated as $1/2 x Fe_2O_3$ content in moles per mole, see Evans and Powell (2015)

Table 2. Experimental run conditions and resulting mineral assemblages, pressure is 3 GPa

	Duration (hrs)	T [(d)] (°C)	Silicate products	Oxides products	capsule material	XMg olivine	stdv	nbr grains	XMg opx	stdv	nbr grains	f_{O2}[(g)] ΔQFM
Ist series : rod sepentinite and olivine trapp												
#1110	12	680	Atg2, Chl, Ol, En	spinel + hem	AuPd	0.95	0.05	4	0.953	0.05	4	3.5
#1111	3	690	Atg2, Chl, Ol, En	spinel + hem	AuPd	0.94	0.09	7	0.95	0.02	3	3.3
#1228[(c)]	10	700	Chl, Ol, En	spinel + hem	AuPd	0.94	0.13	8	0.95	0.05	4	3.6
#1224	10	770	Chl, Ol, En	spinel + hem	AuPd	0.95	0.12	8	0.95	0.03	4	3.5
#1070	6	790	Chl, Ol, En	spinel + hem	AuPd	0.96	0.06	10	0.94	0.06	3	3.9
#262	5	800	Chl, Ol, En	spinel + hem	AuPd	0.97	0.04	5	0.96	0.02	4	4.7
#1273[(c)]	5	900	Ol, En	oxide	AuPd	0.94	0.07	6	0.93	0.12	7	
2nd series : powdered serpentinite and olivine trapp												
#739[(a)]	5	660	Chl, Ol, En	spinel + hem	AuPd	0.94	0.007	4	0.95	0.01	3	3.1
#733	5	850	Ol, En	spinel + hem	AuPd	0.95	0.005	6	0.94	0.94	2	3.7
#735[(b)]	5	850	Ol, En	oxide	AuPd	0.89	0.006	7	0.93	0.01	3	
#737	12	840	Ol, En	n.o.	AuPd	0.90	0.014	5	0.92	0.01	4	
3rd series :powdered serpentinite without olivine trapp												
Effect of the capsule												
#830	12	800	Ol, En	not observed	AuPd[(f)]	0.93	0.00	8	0.94	0.00	12	
#897A	12	≥800	Ol, En	not observed	Au[(f)]	0.96	0.00	7	0.97	0.00	5	
#900A	12	800	Ol, En	spinel + hem	AuPd	0.97	0.008	12	0.94	0.01	10	4.8[(e)]
#900B	12	800	Ol, En	spinel + hem	Au	0.96	0.006	10	0.92	0.01	8	4.1[(e)]
Effect of heating duration												
#869	12	700	Chl, Ol, En	spinel + hem	AuPd	0.97	0.007	6	0.95	0.01	4	4.5[(e)]
#862	12	≤800	Ol, En	spinel + hem	AuPd	0.96	0.009	7	0.95	0.02	6	4.1
#832	12	≥800	Ol, En	spinel	AuPd	0.88	0.05	11	0.94	0.01	7	
#827	24	800	Ol, En	spinel	AuPd	0.90	0.03	14	0.94	0.01	4	
#897B	12	≥800	Ol, En	rare spinel	Au	0.90	0.005	6	0.92	0.01	4	
#860	24	800	Ol, En	spinel	Au	0.92	0.006	20	0.93	0.00	5	

[(a)] 1wt% NaCl added in the starting material

[(b)] 1 wt% FeS added in the starting material

[©] experiment performed using a graphite capsule

[(d)] maximum thermal gradient is of 30°C/mm

[(e)] the f_{O2} of these samples where not considered in Figure 9 because the Kd Fe between olivine and orthopyroxene is too low.

[(f)] νo Mg in the starting material

(g) ΔQFM= log f_{O2}(sample) - log f_{O2}(QFM), with log f_{O2}(QFM) = 82.75 + 0.00484 T - 30681/T - 24.45 log T + 940 P/T - 0.02 P, with T in Kelvins and P in GPa (from O'Neill et al., 1987)

Table 3. chemical compositions of antigorite and dehydration products from EPMA. N= number of analysis.

Experiment	#1110								#1111								#1228						#1224						#1070					
Mineral	Atg2		Chl		Ol		En		Atg		Chl	Ol		En			Chl		Ol		En		Chl		Ol		En		Chl		Ol		En	
n	8		3		4		4		10		1	7		3			2		8		4		4		8		4		4		10		3	
SiO2	43.78	(0.48)	36.36	(1.29)	42.38	(1.39)	59.11	(1.22)	43.30	(0.78)	36.18	42.34	(1.03)	57.40	(1.00)		36.95	(1.49)	41.60	(1.06)	58.01	(1.01)	34.01	(0.63)	42.11	(0.94)	57.46	(1.04)	34.80	(0.89)	42.50	(1.23)	56.80	(0.85)
TiO2	0.03	(0.04)	0.33	(0.47)	0.01	(0.01)	0.01	(0.01)	0.03	(0.04)	0.05	0.04	(0.04)	0.05	(0.06)		0.02	(0.03)	0.03	(0.03)	0.02	(0.04)	0.01	(0.01)	0.06	(0.06)	0.01	(0.02)	0.01	(0.02)	0.03	(0.05)	0.03	(0.03)
Al2O3	1.06	(0.35)	12.43	(0.37)	0.11	(0.07)	1.67	(0.23)	1.47	(0.76)	12.86	0.21	(0.14)	2.58	(0.16)		13.00	(1.21)	0.17	(0.16)	2.59	(0.23)	15.52	(0.57)	0.14	(0.13)	2.41	(0.23)	14.27	(0.73)	0.14	(0.14)	3.00	(0.59)
Cr2O3	0.24	(0.06)	0.72	(0.12)	0.16	(0.05)	0.33	(0.04)	0.15	(0.09)	0.84	0.15	(0.11)	0.24	(0.09)		1.10	(0.17)	0.20	(0.06)	0.24	(0.06)	0.83	(0.16)	0.23	(0.06)	0.20	(0.06)	0.82	(0.09)	0.23	(0.13)	0.30	(0.10)
FeO	2.71	(0.15)	2.62	(0.40)	4.78	(0.46)	3.22	(0.33)	3.06	(0.29)	2.83	5.82	(0.85)	3.68	(0.17)		2.88	(0.04)	6.11	(1.24)	3.02	(0.20)	3.05	(0.19)	4.49	(1.19)	3.55	(0.26)	3.16	(0.13)	4.29	(0.63)	3.08	(0.06)
NiO	0.17	(0.05)	0.17	(0.05)	0.29	(0.06)	0.10	(0.02)	0.16	(0.04)	0.17	0.25	(0.05)	0.11	(0.07)		0.16	(0.00)	0.23	(0.03)	0.13	(0.03)	0.16	(0.04)	0.24	(0.06)	0.11	(0.04)	0.16	(0.11)	0.20	(0.12)	0.11	(0.06)
MnO	0.09	(0.03)	0.03	(0.03)	0.15	(0.03)	0.09	(0.04)	0.06	(0.04)	0.00	0.13	(0.03)	0.09	(0.02)		0.03	(0.04)	0.10	(0.03)	0.06	(0.04)	0.02	(0.03)	0.08	(0.07)	0.10	(0.02)	0.02	(0.02)	0.09	(0.04)	0.08	(0.02)
MgO	39.24	(0.68)	35.18	(0.47)	52.02	(1.41)	36.86	(0.41)	39.15	(0.46)	34.61	51.41	(0.79)	36.79	(0.74)		33.83	(0.41)	50.87	(1.15)	36.28	(0.95)	34.56	(0.27)	52.63	(1.11)	36.02	(0.47)	34.63	(0.51)	52.35	(0.79)	37.20	(2.50)
CaO	0.01	(0.02)	0.15	(0.09)	0.00	(0.00)	0.01	(0.01)	0.01	(0.02)	0.00	0.00	(0.00)	0.03	(0.03)		0.03	(0.02)	0.02	(0.02)	0.07	(0.04)	0.03	(0.02)	0.01	(0.01)	0.03	(0.01)	0.04	(0.07)	0.02	(0.02)	0.04	(0.06)
Total	87.33	(1.01)	88.00	(0.00)	99.91	(0.55)	101.40	(1.12)	87.40	(0.81)	87.55	100.34	(0.69)	100.97	(0.39)		88.00	(0.00)	99.32	(0.66)	100.44	(2.07)	88.18	(0.35)	99.99	(0.77)	99.90	(1.52)	87.91	(0.42)	99.86	(0.70)	100.62	(3.93)
Ions calculated on the basis of 6.824 equivalent oxygens (polysom m=17) for antigorite, 14 for chlorite, 4 for olivine and 6 for orthopyroxene																																		
Si	1.98	(0.01)	3.37	(0.10)	1.01	(0.03)	1.98	(0.02)	1.96	(0.03)	3.37	1.01	(0.02)	1.94	(0.03)		3.42	(0.13)	1.01	(0.02)	1.96	(0.01)	3.16	(0.05)	1.01	(0.01)	1.96	(0.01)	3.24	(0.07)	1.01	(0.02)	1.95	(0.02)
Ti	0.00	(0.00)	0.02	(0.03)	0.00	(0.00)	0.00	(0.00)	0.00	(0.00)	0.00	0.00	(0.00)	0.00	(0.00)		0.00	(0.00)	0.00	(0.00)	0.00	(0.00)	0.00	(0.00)	0.00	(0.00)	0.00	(0.00)	0.00	(0.00)	0.00	(0.00)	0.00	(0.00)
Al	0.06	(0.02)	1.36	(0.05)	0.00	(0.00)	0.07	(0.01)	0.08	(0.04)	1.41	0.01	(0.00)	0.10	(0.01)		1.42	(0.14)	0.00	(0.00)	0.09	(0.00)	1.70	(0.06)	0.00	(0.00)	0.10	(0.01)	1.57	(0.09)	0.00	(0.00)	0.10	(0.01)
Cr	0.01	(0.00)	0.05	(0.01)	0.00	(0.00)	0.01	(0.00)	0.01	(0.00)	0.06	0.00	(0.00)	0.01	(0.00)		0.08	(0.01)	0.00	(0.00)	0.00	(0.00)	0.06	(0.01)	0.00	(0.00)	0.01	(0.00)	0.06	(0.01)	0.00	(0.00)	0.01	(0.00)
Fe	0.10	(0.01)	0.20	(0.03)	0.10	(0.01)	0.09	(0.01)	0.12	(0.01)	0.22	0.12	(0.02)	0.10	(0.01)		0.22	(0.00)	0.12	(0.03)	0.10	(0.01)	0.24	(0.02)	0.09	(0.02)	0.10	(0.01)	0.25	(0.01)	0.09	(0.01)	0.11	(0.02)
Ni	0.01	(0.00)	0.01	(0.00)	0.01	(0.00)	0.00	(0.00)	0.01	(0.00)	0.01	0.00	(0.00)	0.00	(0.00)		0.01	(0.00)	0.00	(0.00)	0.00	(0.00)	0.01	(0.00)	0.00	(0.00)	0.00	(0.00)	0.01	(0.01)	0.00	(0.00)	0.00	(0.00)
Mn	0.00	(0.00)	0.00	(0.00)	0.00	(0.00)	0.00	(0.00)	0.00	(0.00)	0.00	0.00	(0.00)	0.00	(0.00)		0.00	(0.00)	0.00	(0.00)	0.01	(0.00)	0.00	(0.00)	0.00	(0.00)	0.00	(0.00)	0.00	(0.00)	0.00	(0.00)	0.00	(0.00)
Mg	2.65	(0.03)	4.86	(0.09)	1.86	(0.06)	1.84	(0.04)	2.64	(0.03)	4.81	1.83	(0.03)	1.85	(0.04)		4.67	(0.07)	1.84	(0.04)	1.83	(0.01)	4.79	(0.04)	1.88	(0.03)	1.83	(0.01)	4.81	(0.06)	1.86	(0.04)	1.82	(0.00)
Ca	0.00	(0.00)	0.01	(0.01)	0.00	(0.00)	0.00	(0.00)	0.00	(0.00)	0.00	0.00	(0.00)	0.00	(0.00)		0.00	(0.00)	0.00	(0.00)	0.00	(0.00)	0.00	(0.00)	0.00	(0.00)	0.00	(0.00)	0.00	(0.01)	0.00	(0.00)	0.00	(0.00)
O	6.82	(0.00)	14.00	(0.00)	4.00	(0.00)	6.00	(0.00)	6.82	(0.00)	14.00	4.00	(0.00)	6.00	(0.00)		14.00	(0.00)	4.00	(0.00)	6.00	(0.00)	14.00	(0.00)	4.00	(0.00)	6.00	(0.00)	14.00	(0.00)	4.00	(0.00)	6.00	(0.00)
XMg	0.96	0.02	0.96	0.06	**0.95**	0.05	**0.95**	0.05	0.96	0.04	0.96	0.94	0.09	0.95	0.02		0.95	0.01	0.94	0.13	0.95	0.05	0.95	0.03	0.95	0.12	0.95	0.03	0.95	0.02	0.96	0.06	0.94	0.10
XFe	0.04	0.02	0.04	0.06	0.05	0.05	0.05	0.05	0.04	0.04	0.04	0.06	0.09	0.05	0.02		0.05	0.01	0.06	0.13	0.05	0.05	0.05	0.03	0.05	0.12	0.05	0.03	0.05	0.02	0.04	0.06	0.06	0.10
KdFe-Mg Ol/En[1]	**1.05**								**1.13**								**1.19**						**0.87**						**0.78**					

[1] $Kd_{Fe\text{-}Mg}^{Ol/Opx} = (X_{Fe}^{ol} X_{Mg}^{opx}) / (X_{Mg}^{ol} X_{Fe}^{opx})$ see text

Table 3. continued

Experiment	#739						#827				#830				#832				#860				#862			
Mineral	Olivine		Orthopyroxène		Chlorite		Ol		En		Ol		En		Ol		En		Ol		En		Ol		En	
n	4		3		2		18		4		8		12		11		7		20		5		7		6	
SiO2	43.92	(2.28)	56.16	(3.03)	36.98	(5.85)	41.29	(0.81)	55.63	(1.19)	42.42	(1.15)	56.12	(0.88)	41.61	(0.72)	55.90	(1.74)	41.58	(1.11)	52.49	(2.73)	43.16	(0.68)	54.09	(4.17)
TiO2	0.01	(0.01)	0.05	(0.01)	0.02	(0.01)	0.02	(0.02)	0.06	(0.04)	0.00	(0.02)	0.01	(0.04)	0.02	(0.04)	0.02	(0.03)	0.02	(0.03)	0.05	(0.05)	0.02	(0.05)	0.02	(0.03)
Al2O3	0.13	(0.09)	2.74	(1.21)	12.06	(1.67)	0.13	(0.11)	4.44	(0.83)	0.22	(0.20)	3.41	(0.48)	0.13	(0.07)	3.90	(0.81)	0.18	(0.16)	4.47	(0.72)	0.05	(0.05)	2.15	(0.83)
Cr2O3	0.14	(0.04)	0.24	(0.05)	0.85	(0.19)	-	-	-	-	-	-	-	-	-	-	-	-	0.10	(0.12)	0.00	(0.00)	0.08	(0.07)	0.25	(0.10)
FeO	5.62	(0.59)	3.17	(1.20)	3.32	(0.19)	8.57	(2.89)	3.84	(0.50)	6.42	(0.29)	4.27	(0.21)	6.89	(1.51)	4.36	(0.68)	8.00	(0.52)	4.27	(0.75)	4.32	(0.93)	4.05	(1.75)
NiO	0.00	(0.00)	0.00	(0.00)	0.00	(0.00)	0.30	(0.06)	0.19	(0.02)	0.28	(0.09)	0.08	(0.02)	0.32	(0.08)	0.16	(0.05)	0.39	(0.06)	0.13	(0.05)	0.37	(0.05)	0.22	(0.10)
MnO	0.15	(0.04)	0.09	(0.08)	0.04	(0.01)	0.11	(0.04)	0.08	(0.02)	0.11	(0.03)	0.14	(0.03)	0.11	(0.02)	0.10	(0.02)	0.11	(0.02)	0.08	(0.05)	0.12	(0.03)	0.09	(0.01)
MgO	52.54	(2.54)	36.58	(4.89)	35.53	(4.24)	49.34	(2.15)	34.96	(0.53)	50.98	(0.93)	35.63	(1.04)	50.34	(1.48)	35.79	(1.14)	49.06	(1.15)	32.31	(2.16)	54.27	(0.75)	41.04	(3.50)
CaO	0.01	(0.02)	0.03	(0.02)	0.06	(0.03)	0.00	(0.02)	0.08	(0.08)	0.01	(0.02)	0.07	(0.17)	0.02	(0.04)	0.02	(0.03)	0.01	(0.02)	0.22	(0.24)	0.00	(0.03)	0.02	(0.02)
Total	102.55		99.28	(7.66)	89.36	(12.00)	99.77	(0.87)	99.27	(1.54)	100.44	(1.27)	99.73	(0.66)	99.44	(1.29)	100.25	(0.87)	99.45	(1.12)	94.02	(5.49)	102.39	(0.91)	101.93	(1.22)
Ions calculated on the basis of 14 oxygens for chlorite, 4 for olivine and 6 for orthopyroxene																										
Si	1.02	(0.02)	1.93	(0.03)	3.39	(0.08)	1.01	(0.01)	1.81	(0.02)	1.02	(0.02)	1.92	(0.04)	1.02	(0.01)	1.90	(0.06)	1.02	(0.03)	1.90	(0.10)	1.01	(0.01)	1.78	(0.15)
Ti	0.00	(0.00)	0.00	(0.00)	0.00	(0.00)	0.00	(0.00)	0.00	(0.00)	0.00	(0.00)	0.00	(0.00)	0.00	(0.00)	0.00	(0.00)	0.00	(0.00)	0.00	(0.00)	0.00	(0.00)	0.00	(0.00)
Al	0.00	(0.00)	0.11	(0.05)	1.30	(0.01)	0.00	(0.00)	0.18	(0.03)	0.01	(0.01)	0.14	(0.02)	0.00	(0.00)	0.16	(0.03)	0.01	(0.01)	0.19	(0.03)	0.00	(0.00)	0.08	(0.03)
Cr	0.00	(0.00)	0.01	(0.00)	0.06	(0.01)	-	-	-	-	-	-	-	-	-	-	-	-	0.00	(0.00)	0.00	(0.00)	0.00	(0.00)	0.00	(0.00)
Fe	0.11	(0.02)	0.09	(0.03)	0.25	(0.03)	0.18	(0.06)	0.11	(0.01)	0.13	(0.01)	0.12	(0.01)	0.12	(0.04)	0.12	(0.02)	0.17	(0.01)	0.13	(0.02)	0.09	(0.02)	0.11	(0.05)
Ni	0.00	(0.00)	0.00	(0.00)	0.00	(0.00)	0.01	(0.00)	0.01	(0.00)	0.01	(0.00)	0.00	(0.00)	0.01	(0.00)	0.00	(0.00)	0.01	(0.00)	0.00	(0.00)	0.01	(0.00)	0.01	(0.00)
Mn	0.00	(0.00)	0.00	(0.00)	0.00	(0.00)	0.00	(0.00)	0.00	(0.00)	0.00	(0.00)	0.00	(0.00)	0.00	(0.00)	0.00	(0.00)	0.00	(0.00)	0.00	(0.00)	0.00	(0.00)	0.00	(0.00)
Mg	1.83	(0.03)	1.87	(0.12)	4.86	(0.11)	1.80	(0.06)	1.79	(0.03)	1.83	(0.02)	1.81	(0.04)	1.84	(0.06)	1.81	(0.05)	1.80	(0.03)	1.76	(0.08)	1.89	(0.02)	2.01	(0.16)
Ca	0.00	(0.00)	0.00	(0.00)	0.01	(0.00)	0.00	(0.00)	0.00	(0.00)	0.00	(0.00)	0.00	(0.01)	0.00	(0.00)	0.00	(0.00)	0.00	(0.00)	0.01	(0.01)	0.00	(0.00)	0.00	(0.00)
O	4.00		6.00		14.00		4.00	(0.00)	6.00	(0.00)	4.00	(0.00)	6.00	(0.00)	4.00	(0.00)	6.00	(0.00)	4.00	(0.00)	6.00	(0.00)	4.00	(0.00)	6.00	(0.00)
XMg	0.94		0.95		0.95		0.91	0.03	0.94	0.01	0.93	0.00	0.94	0.01	0.89	0.05	0.94	0.01	0.92	0.01	0.93	0.01	0.96	0.01	0.95	0.02
XFe	0.06		0.05		0.05		0.09	0.03	0.06	0.01	0.07	0.00	0.06	0.01	0.12	0.05	0.06	0.01	0.08	0.01	0.07	0.01	0.04	0.01	0.05	0.02
KdFe-Mg Ol/E	**1.24**						**1.59**				**1.11**				**1.90**				**1.24**				**0.82**			

Table 3.
continued

Experiment	#869						#897A				#897B				#900A				#900B			
Mineral	Chl		Ol		En		Ol		En		Ol		En		Ol		En		Ol		En	
n	7		6		4		7		5		6		3		12		10		10		8	
SiO2	34.70	(3.42)	45.80	(2.95)	58.07	(1.82)	43.04	(0.47)	57.63	(1.28)	41.29	(0.51)	57.97	(1.89)	43.37	(0.87)	57.95	(0.85)	43.55	(1.14)	56.77	(0.66)
TiO2	-0.01	(0.03)	0.00	(0.03)	0.00	(0.03)	0.01	(0.03)	0.09	(0.03)	0.00	(0.02)	0.19	(0.02)	0.02	(0.05)	0.00	(0.02)	0.00	(0.03)	0.03	(0.03)
Al2O3	8.94	(2.45)	0.29	(0.20)	1.65	(0.47)	0.12	(0.09)	4.97	(0.49)	0.06	(0.05)	4.89	(0.25)	0.06	(0.08)	2.76	(0.27)	0.13	(0.19)	3.13	(0.30)
Cr2O3	0.57	(0.16)	0.13	(0.04)	0.26	(0.12)	0.08	(0.12)	0.51	(0.11)	0.05	(0.02)	0.82	(0.14)	0.06	(0.09)	0.12	(0.06)	0.05	(0.05)	0.17	(0.07)
FeO	2.15	(0.11)	2.62	(0.65)	3.48	(0.84)	3.90	(0.09)	2.39	(0.10)	9.92	(1.01)	5.31	(0.52)	2.88	(0.81)	4.12	(0.42)	4.05	(0.68)	5.26	(0.70)
NiO	0.29	(0.04)	0.36	(0.16)	0.13	(0.05)	0.32	(0.03)	0.08	(0.02)	0.33	(0.05)	0.07	(0.03)	0.37	(0.05)	0.14	(0.02)	0.36	(0.02)	0.14	(0.02)
MnO	0.05	(0.02)	0.11	(0.03)	0.12	(0.03)	0.10	(0.03)	0.08	(0.03)	0.13	(0.04)	0.10	(0.02)	0.11	(0.03)	0.10	(0.04)	0.09	(0.02)	0.11	(0.03)
MgO	30.45	(3.88)	50.96	(3.40)	37.26	(1.58)	53.22	(0.73)	36.80	(1.25)	48.62	(0.70)	35.82	(1.60)	55.28	(1.30)	36.80	(0.39)	53.32	(1.01)	35.71	(0.64)
CaO	0.16	(0.21)	0.03	(0.02)	0.02	(0.03)	0.01	(0.02)	0.04	(0.01)	0.01	(0.02)	0.07	(0.05)	0.02	(0.02)	0.01	(0.03)	0.01	(0.01)	0.03	(0.03)
Total	77.32	(7.92)	100.30	(2.07)	100.99	(2.68)	100.80	(0.41)	102.59	(2.08)	100.41	(1.19)	105.24	(3.51)	102.17	(1.42)	102.00	(0.81)	101.56	(0.59)	101.34	(0.65)
Ions calculated on the basis of 14 oxygens for chlorite, 4 for olivine and 6 for orthopyroxene																						
Si	5.19	(0.27)	1.10	(0.08)	1.96	(0.04)	1.02	(0.02)	1.91	(0.00)	1.01	(0.00)	1.94	(0.01)	1.01	(0.02)	1.96	(0.03)	1.37	(0.04)	1.46	(0.02)
Ti	0.00	(0.00)	0.00	(0.00)	0.00	(0.00)	0.00	(0.00)	0.00	(0.00)	0.00	(0.00)	0.01	(0.00)	0.00	(0.00)	0.00	(0.00)	0.00	(0.00)	0.00	(0.00)
Al	1.57	(0.35)	0.01	(0.01)	0.07	(0.02)	0.00	(0.00)	0.19	(0.02)	0.00	(0.00)	0.10	(0.00)	0.05	(0.01)	0.00	(0.00)	0.00	(0.00)	0.05	(0.01)
Cr	0.07	(0.02)	0.00	(0.00)	0.00	(0.00)	0.00	(0.00)	0.01	(0.00)	0.00	(0.00)	0.01	(0.00)	0.00	(0.00)	0.00	(0.00)	0.00	(0.00)	0.00	(0.00)
Fe	0.27	(0.02)	0.05	(0.01)	0.10	(0.02)	0.08	(0.00)	0.07	(0.00)	0.20	(0.02)	0.15	(0.02)	0.06	(0.02)	0.11	(0.01)	0.11	(0.02)	0.11	(0.02)
Ni	0.04	(0.01)	0.01	(0.00)	0.00	(0.00)	0.01	(0.00)	0.00	(0.00)	0.01	(0.00)	0.00	(0.00)	0.01	(0.00)	0.00	(0.00)	0.01	(0.00)	0.00	(0.00)
Mn	0.01	(0.00)	0.00	(0.00)	0.00	(0.00)	0.00	(0.00)	0.00	(0.00)	0.00	(0.00)	0.00	(0.00)	0.00	(0.00)	0.00	(0.00)	0.00	(0.00)	0.00	(0.00)
Mg	6.77	(0.34)	1.83	(0.09)	1.87	(0.07)	1.89	(0.02)	1.81	(0.02)	1.78	(0.02)	1.79	(0.02)	1.92	(0.01)	1.86	(0.04)	2.51	(0.04)	1.37	(0.02)
Ca	0.02	(0.03)	0.00	(0.00)	0.00	(0.00)	0.00	(0.00)	0.00	(0.00)	0.00	(0.00)	0.00	(0.00)	0.00	(0.00)	0.00	(0.00)	0.00	(0.00)	0.00	(0.00)
O	14.00	(0.00)	4.00	(0.00)	6.00	(0.00)	4.00	(0.00)	6.00	(0.00)	4.00	(0.00)	6.00	(0.00)	4.00	(0.00)	6.00	(0.00)	4.00	(0.00)	6.00	(0.00)
XMg	0.96	0.00	0.97	0.01	0.95	0.01	0.96	0.00	0.97	0.00	0.90	0.01	0.92	0.01	0.97	0.01	0.94	0.01	0.96	0.01	0.92	0.01
XFe	0.04	0.00	0.03	0.01	0.05	0.01	0.04	0.00	0.04	0.00	0.10	0.01	0.08	0.01	0.03	0.01	0.06	0.01	0.04	0.01	0.08	0.01
KdFe-Mg Ol/En			**0.55**				**1.12**				**1.38**				**0.47**				**0.52**			

Table 4. Example of compositions of oxide minerals from EPMA.

Exp. Number	#1111		#1070			#1110				#1224		#1228		#M827		#M832		#M862			#M869	
Mineral	Mg	Hem	Mg	Chr	Hem	Mg	Chr	SP	Hem	Mg	Hem	Mg	Hem	Chr	SP	Chr	Mg	Hem	Chr	SP	Hem	Mg
nbr points	10	4	7	1	3	9	4	1	9	9	11	16	1	5	3	4	5	4	2	1	7	3
Fe	2.88 0.04	1.96 0.02	2.81 0.11	1.81	1.94 0.03	2.84 0.12	1.79 0.11	0.66	1.96 0.02	2.68 0.08	1.97 0.01	2.94 0.05	1.94	1.87 0.14	0.64 0.25	1.85 0.19	2.75 0.05	1.92 0.02	1.58 0.02	0.26	1.97 0.01	2.71 0.44
Mg	0.08 0.04	0.01 0.01	0.12 0.10	0.06	0.01 0.02	0.03 0.03	0.10 0.05	0.39	0.00 0.00	0.28 0.08	0.00 0.00	0.01 0.00	0.01	0.10 0.07	0.96 0.59	0.09 0.02	0.15 0.03	0.01 0.01	0.58 0.01	0.79	0.02 0.01	0.20 0.12
Al	0.00 0.01	0.00 0.00	0.00 0.00	0.01	0.00 0.00	0.01 0.01	0.03 0.03	0.93	0.00 0.00	0.01 0.01	0.00 0.00	0.00 0.00	0.00	0.02 0.03	0.19 0.42	0.02 0.01	0.02 0.02	0.04 0.02	0.18 0.01	1.13	0.00 0.01	0.01 0.00
Cr	0.04 0.03	0.02 0.01	0.06 0.05	0.98	0.04 0.02	0.11 0.08	0.95 0.04	0.99	0.03 0.02	0.03 0.02	0.01 0.01	0.04 0.05	0.04	0.84 0.10	0.20 0.45	0.90 0.18	0.06 0.05	0.02 0.01	0.59 0.00	0.80	0.01 0.00	0.03 0.03
Mn	0.00 0.00	0.00 0.00	0.01 0.01	0.10	0.00 0.00	0.01 0.01	0.09 0.01	0.02	0.00 0.00	0.00 0.00	0.00 0.00	0.00 0.00	0.00	0.09 0.02	0.02 0.01	0.09 0.01	0.01 0.01	0.00 0.00	0.04 0.00	0.02	0.00 0.00	0.01 0.01
Ti	0.00 0.00	0.00 0.00	0.00 0.00	0.04	0.00 0.00	0.01 0.01	0.03 0.01	0.00	0.00 0.00	0.00 0.00	0.00 0.00	0.01 0.00	0.00	0.04 0.00	0.58 0.80	0.04 0.00	0.01 0.00	0.01 0.00	0.00 0.00	0.00	0.00 0.00	0.00 0.00
Cations sum	3.00	2.00	3.00	3.00	2.00	3.00	3.00	3.00	2.00	3.00	2.00	3.00	2.00	3.00	3.00	3.00	3.00	2.00	3.00	3.00	2.00	3.00

Table 5 End member thermodynamic data used for calculating oxygen fugacity.

	ΔHf ° (298)	S_T	Heat Capacity				Vo	Ko	α
	(J/mol)	J/K/mol	a (x1E3)	b (x1E-2)	c (x1E3)	d (x1E3)	(m^3/mol)	(Pa)	
Fayalite	-1478220	151	0.2011	1.733	-1960.6	-0.9009	4.63E-05	1.33E+11	5.05E-05
Forsterite	-2171850	95.1	0.2333	0.1494	-603.8	-1.8697	4.37E-05	1.25E+11	6.13E-05
Enstatite	-3090260	132.5	0.3562	-0.299	-596.9	-3.1853	6.26E-05	1.07E+11	5.05E-05
Ferrosilite	-2388750	190.6	0,393 *	-0.6579	1290.1	-4.058	6.59E-05	1.01E+11	6.32E-05
Hematite	-825730	87.4	0,17 *	0	-2257.2	-0.6576	3.03E-05	2.00E+11	5.99E-05
Magnetite	-1115550	146.1	0,28 *	-0.7204	-1926.2	-1.6557	4.45E-05	1.85E+11	6.96E-05
Iron (fcc)	0	27.32	0.0462	1,2 *	723.1	-0.5562	7.09E-06	1.86E+11	7.46E-05
O_2	0	205.15	0.0483	-0.0691	499.2	-0.4207			
Quartz	-910880	41.5	0.1107	-0.5189	0.0	-1.1283	2.27E-05	7.50E+10	6.50E-06

All data taken from Holland and Powell (1998), except a few Cp terms (*) that were modified in order to take into account for phase transitions, based on comparison with Perplex calculations. $Cp = a + bT + cT^{-2} + dT^{-0.5}$. A Murnaghan equation of state (like in Holland and Powell, 1998) is used to calculate f_{O2} using Excell software.

Activities were calculated assuming an ideal solid solution for pyroxene, and regular solid solution for olivine, whereby $a^{olivine}_{Mg2SiO4}$ and $a^{olivine}_{Fe2SiO4}$ are $X_{Mg}^2.\gamma_{Mg}$ and $X_{Fe}^2.\gamma_{Fe}$ respectively, where X_{Fe}=Fe/(Fe+Mg) and the activity coefficients for olivine are determined from $RT \ln \gamma_a = W^{ol} (1-X_a)^2$ with W^{ol} = 4200 J/atom (Holland and Powell, 1998). The activity coefficient γ in orthopyroxene is equal to 1. The activity coefficient for Fe_2O_3 in hematite is taken as unity as this phase was found to be very pure in composition (see Table 4).